

OPTIMIZATION OF 2×2 COUPLERS FOR OPTICAL FREQUENCY
DOMAIN REFLECTOMETRY

by

Tianyuan Xue

A thesis submitted in conformity with the requirements
for the degree of Master of Applied Science
Graduate department of Electrical and Computer Engineering
University of Toronto

© Copyright 2020 by Tianyuan Xue

Abstract

Optimization of 2×2 Couplers for Optical Frequency Domain Reflectometry

Tianyuan Xue

Master of Applied Science

The Edward S. Rogers Sr. Department of Electrical and Computer Engineering

University of Toronto

2020

This thesis demonstrates broadband, low-loss 2×2 couplers on a silicon photonics platform for chip-scale implementations of optical frequency domain reflectometers (OFDRs). Silicon nitride curved directional couplers and multimode interference couplers were designed, optimized, and evaluated for the O-band near a wavelength of 1310nm. Both types of couplers achieved a 1dB imbalance bandwidth of >100nm around 1310nm in both candidates. However, the curved directional coupler had negligible loss, while the multimode interference coupler had a 1dB excess loss bandwidth of >40nm around 1310nm. The results demonstrate the suitability of the silicon nitride-on-silicon platform for optical frequency domain reflectometry applications and builds a foundation towards a fully integrated photonic OFDR circuit.

Acknowledgements

I would like to first thank my supervisor Prof. Joyce Poon who laid the groundwork for this research, who also provided the expertise and support that made this thesis possible.

Also, I would like to thank the other members and alumni of the group, Dr. Jason Mak, Dr. Zheng Yong, Torrey Thiessen, Fu Der Chen, Junho Jeong, Dr. Youngho Jung, Dr. Wesley Sacher, Ilan Almog, Thomas Lordello, Dr. Jared Mickelson, Yisu Yang and Antoine Bois for their assistance and support.

I would also like to thank Dr. Doug Baney and Dr. Greg Vanwiggeren at Keysight and the Natural Sciences and Engineering Research Council of Canada for funding this project.

I would also like to express thanks to AMF formerly known as IME A*Star for their work fabricating the devices I designed.

Lastly, I would like to thank my parents and grandparents for their emotional support throughout the years.

Table of Contents

Chapter 1	1
1.1. Theory of operation	4
1.2. Polarization Diverse OFDR	6
1.3. Spatial Resolution	7
1.4. Maximum range	8
1.5. Role of 2×2 couplers	9
1.5.1. Balanced Detection	9
1.5.2. Reflection Isolation	10
1.6. Thesis Outline	11
Chapter 2	12
2.1. SiN-on-Si Platform	13
2.2. Waveguide dimensions	14
2.2.1. Polarizer	15
2.3. General Devices	15
2.3.1. Edge coupler	16
2.3.2. Interlayer Transitions	17
2.3.3. Ge Photodetector	19
2.4. Photonic OFDR System Overview	20
2.5. Summary	21
Chapter 3	22
3.1. Design Goals	23
3.2. Comparison of 2×2 couplers	24
3.2.1. Multimode Interferometer (MMI)	25
3.2.2. Directional Coupler	30
3.2.3. Adiabatic coupler	39
3.3. Comparison of 2×2 Coupler Options	39
3.4. Conclusion	40

Chapter 4	41
4.1. Test Structures	41
4.1.1. Polarization Calibration Structures	41
4.1.2. Edge coupler Calibration Structures	42
4.1.3. Waveguide Cutback Structures	42
4.1.4. Transition Cutback Structures	43
4.1.5. MMI Cutback Structure	43
4.1.6. Unbalanced Mach-Zehnder Interferometer	44
4.1.7. Germanium photodetector	48
4.2. Measurement setup	48
4.3. Conclusion	49
Chapter 5	50
5.1. Waveguide Propagation	50
5.2. Interlayer Transitions	52
5.3. Photodetector Responsivity	53
5.4. MMI Measurements	53
5.5. Directional Coupler Measurements	55
5.6. Discussion	58
5.7. Conclusion	59
Chapter 6	61
6.1. Conclusion	61
6.2. Future Work	63

List of Tables

Table 2.1: <i>Power coupling between SMF28 fibre mode and minimum dimensions on SiN and Si.....</i>	16
Table 3.1: <i>MMI parameters</i>	28
Table 3.2: <i>Curved Directional coupler parameters.....</i>	37
Table 6.1: <i>Comparison table for 2×2 couplers on SOI platforms</i>	62

List of Figures

Figure 1.1: The cross section of a typical SiN-on-Si platform. TiN is titanium nitride, which is used for heating elements. Ge is germanium, which is used for photodetection	3
Figure 1.2: A diagram of an OFDR implementation. Light from a wavelength-swept tunable laser source enters a coupler and is split to a path going to the device under test (DUT) and a path going to the photodetector (PD) as the local oscillator. The light going to the DUT passes through a circulator, and the reflection from the DUT enters the circulator and is directed to the PD. The local oscillator and reflection is mixed at the PD using a second 2×2 coupler. A fast Fourier transform (FFT) is performed on the electrical output of the PD. The positions of reflection sites are deduced from the FFT.	5
Figure 1.3: A diagram of external polarization management assembly; the TE polarized light coming from the “TM” probe port under goes polarization rotation (PR) into the orthogonal polarization, and a temporal delay τ is applied through a delay line, and combined with the TE polarized light from the TE probe port in the polarization beam splitter (PBS) and sent to the device under test (DUT), resulting in the TM polarized light in the combined beam containing a temporal delay τ relative to the TE polarized light. The 2 polarizations in the back reflections from the DUT is split by the PBS, with the TM component acquiring an additional delay τ before it reenters the OFDR chip. The TM \rightarrow TM and TE \rightarrow TM reflections will be collected at the “TM” probe port with an applied temporal delay of 2τ and τ respectively. The TE \rightarrow TE and TM \rightarrow TE reflections will be collected at the TE probe port with an applied temporal delay of 0 and τ respectively. The difference in temporal delays translate to a spatial offset after the interference is Fourier transformed, multiplexing the terms of the reflection’s Jones matrix spatially.	7
Figure 1.4: A diagram of a 2×2 coupler. t_b , t_c are the bar and cross port coupling coefficient, respectively.....	9
Figure 1.5: A diagram showing balanced photodetection. E_{DUT} is the back reflections from the device under test (DUT), E_{LO} is the local oscillator (LO). The outputs at port 3 and 4 are incident on photodetectors generating a photocurrent of I_3 and I_4 . The output of the balanced detection is the difference between the photocurrents I_3 and I_4	9

Figure 1.6: A diagram of 2×2 coupler acting as a circulator. The incoming signal from the tunable laser source enters through port 1 and is routed to ports 3 and 4. Port 3 is connected to the device under test (DUT). Back reflections from the DUT enter through port 3 and is routed to ports 1 and 2. Back reflections are isolated in port 2.	10
Figure 2.1: Cross-section of the multi-layer SiN-on-Si platform used in this work (not to scale). $t_{\text{Si}} = 150\text{nm}$, $t_{\text{SiN}} = 400\text{nm}$, $t_{\text{Spacer}} = 200\text{nm}$, $t_{\text{BOX}} = 2\mu\text{m}$, $t_{\text{Ge}} = 500\text{nm}$	13
Figure 2.2: Effective index of supported waveguide modes at 1310nm, Si strip waveguide with a height of 220nm and refractive index of 3.507 (left) and SiN strip waveguide with a height of 400nm and refractive index of 1.905 (right).....	14
Figure 2.3: The simulated transmission of TE ₀ and TM ₀ modes in a Si strip waveguide with a height of 220nm and width of 350nm through a 90° bend with a radius of 10μm	15
Figure 2.4: The geometric definition of the inverse spot size converter and the simulated TE ₀ mode profile at various points along the device. W_{tip} is the width of the tip, L_{taper} is the length of the linear taper from the tip width to the nominal waveguide widths of SiN (750nm) and Si (350nm)...	16
Figure 2.5: (left) The L_{taper} sweep results for the TE ₀ mode transmission for the SiN inverse taper at 1310nm. (right) The wavelength sweep for TE ₀ mode transmission for the SiN inverse taper with $L_{\text{taper}} = 500\mu\text{m}$	17
Figure 2.6: The geometric definition for interlayer transition between the SiN and Si layers and the simulated TE ₀ mode profile at various points along the device. $W_{\text{Si,tip}}$ and $W_{\text{SiN,tip}}$ are the tip widths of the Si and SiN tapers respectively, and L_{taper} is the length of the linear taper in the interlayer transition.....	18
Figure 2.7: (left) L_{taper} sweep results for the TE ₀ mode transmission of the interlayer transition. (right) FDTD simulation results for the TE ₀ mode transmission of the interlayer transition with $L_{\text{taper}} = 100\mu\text{m}$	18
Figure 2.8: Cross-sectional view of the Ge Photodetector. The silicon (Si) and germanium (Ge) are P and N doped respectively to form a P-I-N junction. P+ and N+ doping are used create ohmic contacts with the metal.	19
Figure 2.9: The electric field intensity profile inside the Ge photodetector as simulated by the FDTD method.	20

Figure 2.10: A schematic of OFDR implementation on a SiN-on-Si platform using edge couplers, interlayer transitions, polarization filters, photodetectors and 2×2 couplers. The light from the tunable laser source (TLS) is coupled into the SiN layer through the edge couplers, goes towards the 2×2 coupler, and is split into the device under test (DUT) and the local oscillator (LO). The back reflected signal from the DUT combines with the LO in the second 2×2 coupler, and the mixed signals are transited down through interlayer transitions to the Si layer, where it undergoes polarization filtering, and is detected by the Ge photodetectors.	20
Figure 3.1: Schematic overview of 2×2 coupler. T_{bar} , T_{cross} are the bar and cross port transmissions respectively.....	23
Figure 3.2: A diagram of slab modes in slab region of the MMI recreated from [44]. W_{eff} is the effective width of the slab modes, and W_{MMI} is the width of the slab region.....	25
Figure 3.3: The geometric definition of proposed multimode interferometer (MMI). L_{MMI} and W_{MMI} are the length and width of the slab region of the MMI. L_{taper} is the taper length of the entry and exit waveguides from the nominal waveguide widths to the entry waveguide width (W_{entry}). y_{ofs} is the centerline offset between entry and exit waveguides and the center of the slab region.	27
Figure 3.4: Initial parameters W_{MMI} , $W_{\text{eff}}/W_{\text{MMI}}$ sweep in EME solver for calculated worst case single port rejection ratio (SPRR, left), and T_{refl} (right) in the target wavelength range (1260-1360nm) Star denotes the initial parameters for MMI design.	28
Figure 3.5: Plots of the optimized MMI design transmissions (blue) and splitting ratio (orange), for the nominal design (top left), and under different potential fabrication variances, index (± 0.02 , top right), waveguide height($\pm 40\text{nm}$, bottom left), waveguide width($\pm 75\text{nm}$, bottom right).....	29
Figure 3.6: The geometric definition of a directional coupler. L_c is the length of the coupling region, s is the centerline separation between the two waveguides in the coupling region.	30
Figure 3.7: Plot of $\frac{1}{\kappa} \frac{d\kappa}{d\lambda}$ against waveguide separation for a symmetric directional coupler at 1310nm	32
Figure 3.8: Plots of the optimized symmetric directional coupler design transmissions (blue) and splitting ratio (orange), for the nominal design (top left), and under different potential fabrication variances, index (± 0.02 , top right), waveguide height($\pm 40\text{nm}$, bottom left), waveguide width($\pm 75\text{nm}$, bottom right)	32

Figure 3.9: The geometric definition of a curved coupling region. R_c is the centerline bend radius of the coupling region, L_c is the length of the coupling region traversing an angle of θ , s is the centerline separation between the waveguides in the coupling region.	34
Figure 3.10: Calculated bar and cross port transmissions for the curved coupler with $R_c = 79.3\mu\text{m}$, $L_c = 20.1\mu\text{m}$	35
Figure 3.11: Plot of coupling ratio (left) and its derivative with respect to wavelength (right) at 1310nm. Star indicates the optimized parameters.	36
Figure 3.12: Calculated bar and cross port transmissions of curved coupler with $R_c = 91.8\mu\text{m}$, $L_c = 27.2\mu\text{m}$	37
Figure 3.13: Plots of the optimized curved coupler design transmissions (blue) and splitting ratio (orange), for the nominal design (top left), and under different potential fabrication variances, index (± 0.02 , top right), waveguide height($\pm 40\text{nm}$, bottom left), waveguide width($\pm 75\text{nm}$, bottom right)	38
Figure 3.14: A comparison of designed 2×2 couplers on the basis of single port rejection ratio (SPRR) and losses accrued from isolating the back reflection from the DUT (T_{refl}). Stars are the nominal designs, and dots are performances after applying fabrication variations in the index, waveguide height, and waveguide width.	39
Figure 4.1: The layout of a polarization calibration structure	41
Figure 4.2: The layout of waveguide cutback spiral structures labelled (1, 2, 3, 4) have relative pathlength differences of (0, 1.2, 2.4, 3.6)cm.	42
Figure 4.3: The layout of interlayer transition cutback structure labeled (1, 2, 3, 4) have (12, 38, 58, 78) interlayer transitions	43
Figure 4.4: The layout of MMI cutback structures in bar and cross port configurations labeled (1, 2, 3) have (3, 7, 10) consecutive MMIs	43
Figure 4.5: The unbalanced Mach Zehnder interferometer (UMZI) test structure. Top: Layout representation, Bottom: Schematic representation, where In1, In2 are the input ports 1 and 2, respectively and Out1, Out2 are the output ports 1 and 2, respectively. ΔL is the excess path length between the longer arm and the shorter arm of the UMZI structure.	44

Figure 4.6: Simulated group index of SiN strip waveguide as defined in Chapter 2. Dots are calculated interferogram cycles with $\Delta L = 420\mu\text{m}$	47
Figure 4.7: The layout of a 2×2 PD test structure.....	48
Figure 4.8: Schematic representation of the measurement setup. DUT: device under test TLS: Tunable laser source; PC: polarization controller; SM: source meter; PA: Polarization analyzer; OPM: optical power meter.....	49
Figure 5.1 (left) Plot of interpolated waveguide propagation losses for SiN and Si strip waveguides. (right) Raw cutback measurements for SiN and Si strip waveguide spirals at 1310nm	51
Figure 5.2: (left) Plot of interpolated interlayer transition insertion loss. (right) Raw cutback measurements of interlayer transition test structures at 1310nm.....	52
Figure 5.3: The measured Ge PD responsivity as a function of wavelength.....	53
Figure 5.4: MMI characterization results. (top left) cutback characterization (top right) PD characterization (bottom left) raw measurements of bar port cutback measurements at $1.27\mu\text{m}$, $1.31\mu\text{m}$, $1.34\mu\text{m}$ (bottom right) raw measurements of cross port cutback measurements at $1.27\mu\text{m}$, $1.31\mu\text{m}$, $1.34\mu\text{m}$	54
Figure 5.5: Plots of (left) T_{refl} (right) SPRR calculated from the photodetector characterization.	55
Figure 5.6: Plot of raw data from unbalanced Mach Zehnder interferometer measurement, Blue and red dots indicate the peaks and troughs of the interferogram.....	56
Figure 5.7: Plot of curved directional coupler characterization results. (left) unbalanced Mach Zehnder interferometer characterization, (right) photodetector characterization	57
Figure 5.8: Plot of (left) T_{refl} (right) SPRR calculated from the photodetector characterization.....	58
Figure 5.9: Plot of measured unbalanced Mach Zehnder interferometer interference spectra. Green and red dots used to visualize the peaks and troughs (left) Without polarization analyzer (right) With polarization analyzer.....	59
Figure 6.1: Schematic of hybrid configuration of 2×2 couplers for OFDR with the curved directional coupler (DC) routing the light from the tunable laser source (TLS) to the device under test (DUT) and isolating the back reflections from the DUT. and the multimode interferometer (MMI) facilitating the interference between the reflections and the local oscillator (LO).	63

Figure 6.2: Schematic of on chip polarization diversity achieved with integrated polarization splitter rotator (PSR). (top) external bulk optic requirements. Light from the tunable laser source (TLS) is split into 2 paths, with one path connected to a delay line to apply a temporal delay τ (TLS_{delay}) relative to the other path (TLS_{no delay}). (bottom) photonic circuit: the light travels from TLS_{delay} and TLS_{no delay} and is routed towards the device under test (DUT) through the PSR, which converts the TLS_{delay} into the TM polarization. The two polarizations in the back reflections from the DUT are separated by the PSR, and interfered with the local oscillator on the top (originating from TLS_{delay}) and bottom (originating from TLS_{no delay}) branches of the OFDR. On the top branch, the TE→TM and TM→TM reflections will have a relative applied delay of $-\tau$ and 0 to the top branch LO respectively. On the bottom branch, the TE→TE and TM→TE reflections will have a relative applied delay of 0 and τ to the bottom branch LO respectively. The different relative temporal delay in each branch translates to a spatial offset after the interference signal is Fourier transformed, multiplexing the different terms of the reflection's Jones matrix spatially. 64

List of Abbreviations

DC	<i>Directional Coupler</i>
DFT	<i>Discrete Fourier Transform</i>
DUT	<i>Device Under Test</i>
EME	<i>Eigen-mode Expansion</i>
ER	<i>Extinction Ratio</i>
FDTD	<i>Finite-Difference Time-Domain</i>
Ge	<i>Germanium</i>
LO	<i>Local Oscillator</i>
LPCVD	<i>Low Pressure Chemical Vapor Deposition</i>
MMI	<i>Multimode Interferometer</i>
OFDR	<i>Optical Frequency Domain Reflectometry</i>
PD	<i>Photodetector</i>
PDL	<i>Polarization Dependent Loss</i>
PECVD	<i>Plasma Enhanced Chemical Vapor Deposition</i>
Si	<i>Silicon</i>
SiN	<i>Silicon Nitride</i>
SiN-on-Si	<i>Silicon Nitride-on-Silicon</i>
SOI	<i>Silicon-on-Insulator</i>
SPRR	<i>Single Port Rejection Ratio</i>

TE	<i>Transverse-Electric</i>
TiN	<i>Titanium Nitride</i>
TLS	<i>Tunable Laser Source</i>
TM	<i>Transverse-Magnetic</i>
UMZI	<i>Unbalanced Mach-Zehnder Interferometer</i>

Chapter 1

Introduction

Silicon (Si) for integrated photonics has been a topic of intense interest and research in the past decade. Its suitability as a platform for photonics lies in its transparency in the telecommunication wavelengths, opening applications for optical interconnect in telecommunication and computing systems. [1]–[4] Si photonic platforms have a high refractive index contrast between the waveguide core (usually made of Si) and the cladding, which is often silicon dioxide (SiO_2). This results in highly confined optical modes, which leads to miniaturization of device dimensions. Si photonics leverage mature CMOS compatible fabrication technologies and expertise that have developed alongside the microelectronics industry over the last 60 years and has recently developed into a foundry model providing inexpensive fabrication services for highly integrated Si photonic circuits for research and development as well as commercial use. [5]–[7] While the indirect bandgap of Si prevents efficient on chip lasers, there have been demonstrations of bonding III-V to overcome this issue. [8], [9] The doping of Si enables optoelectronic integration in the form of phase modulation through the carrier dispersion effect, and the epitaxial growth of Ge enables the realization of photodetectors in the telecommunication window. [10], [11] These factors all culminate in making Si photonics a highly flexible and miniaturized platform capable of integrating passive devices, modulators, and detectors all on a single monolithic chip.

In the recent years, integration of silicon nitride (SiN) on the traditional silicon-on-insulator (SOI) photonic platform have garnered a great deal of interest due to the passive properties of SiN. [12], [13] SiN can handle higher powers, owing to its negligible two-photon absorption and Kerr coefficient. [14] The lower index contrast of SiN compared to Si makes SiN waveguides less dispersive, more tolerant to fabrication variations, and suffer lower losses due to sidewall roughness when compared to Si waveguides. [12] The lower thermo-optic coefficient also makes SiN devices less sensitive to temperature. [12] By integrating SiN on a SOI platform, a photonic circuit can gain access to the superior passive properties of SiN while retaining the active capabilities of Si, reaping the best of both worlds. SiN-on-Si photonics platforms have become more popular as several open foundries that offer MPW services has integrated of SiN into their photonic platforms. [13] A typical SiN-on-Si platform looks like Figure 1.1 with the metal layers and vias for dense optoelectronic integration. SiN deposition done through either the Low Pressure Chemical Vapor Deposition (LPCVD) or Plasma Enhanced Chemical Vapor Deposition (PECVD) process, the latter of which is more easily compatible with active devices requiring doping profiles due to its lower deposition temperature ($<400^{\circ}\text{C}$). [12]

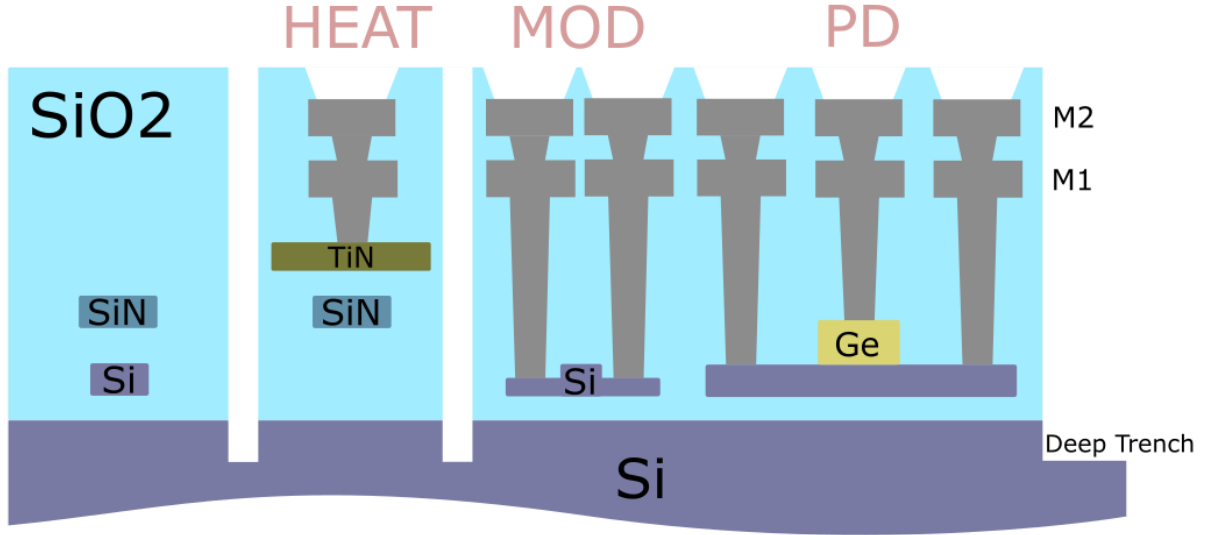


Figure 1.1: The cross section of a typical SiN-on-Si platform. TiN is titanium nitride, which is used for heating elements. Ge is germanium, which is used for photodetection

The high integration density and electronic integration of integrated photonics offer an unprecedented opportunity for the miniaturization of technologies that traditionally have only existed in bulk optic implementations such as optical gyroscopes, light imaging, distance and ranging (LIDAR), and quantum optics. [15]–[17] Through integration on a Si photonics platform, these technologies stand to benefit from the scalable production, robustness, and miniaturization that only integrated optics can offer.

One technology ripe for photonic integration is optical reflectometry, which is a diagnostic technique with widespread applications ranging from optical device diagnostics, distributed monitoring, to medical imaging under the name of optical coherence tomography.[18]–[21] There are several techniques that fall under the category of optical reflectometry. The first is optical time domain reflectometry (OTDR), which sends a pulse of light and times the return pulses to locate reflections. The second is optical frequency domain reflectometry (OFDR), which utilizes interference between a reference arm and a probe arm as the optical frequency is swept to compute the locations of reflections. The third is optical low coherence reflectometry (OLCR), which utilizes white light

interferometry to locate reflections with high precision by tuning the reference arm. Each has different strengths and weaknesses in terms of maximum distance, spatial resolution, and speed. OTDR has a maximum range on the order of kilometers with resolution on the order of meters. [20], [22] OLCR has a maximum range on the order of meters and resolution on the order of microns.[23], [24]. OFDR offers a compromise between the two by offering submillimeter resolution in a range on the order of hundreds of meters and finds application specifically in optical diagnostics of photonic wafer and chips due to its superior measurement speed and dynamic range [25], [26]. Without the need for ultra-high-speed electronics as in OTDR or the shifting reference arm as in OLCR, OFDR stands out as the best candidate for integration on a nanophotonic platform.

An integrated photonics implementation of OFDR can, in addition to the usual advantages in terms of miniaturization, add robustness and lowered costs compared to the bulk optic implementations, also present a unique opportunity in enabling wafer level diagnostics by directly integrating the OFDR test circuits into the wafer under test. This would enable rapid optical characterization of the wafer in reflection without the need for a transmission port.

In this chapter, we will outline the general operating principle of OFDR, talk about the important roles 2×2 couplers play in the realization of an OFDR system implemented on a SiN-on-Si platform and conclude with an overview of the organization of the thesis.

1.1 Theory of operation

The OFDR technique analyzes and locates the reflections coming back from the device under test (DUT) by interfering the reflections with a signal coming from the reference arm, denoted as the local oscillator (LO) as the optical source frequency is swept. The analysis presented below is taken from [26].

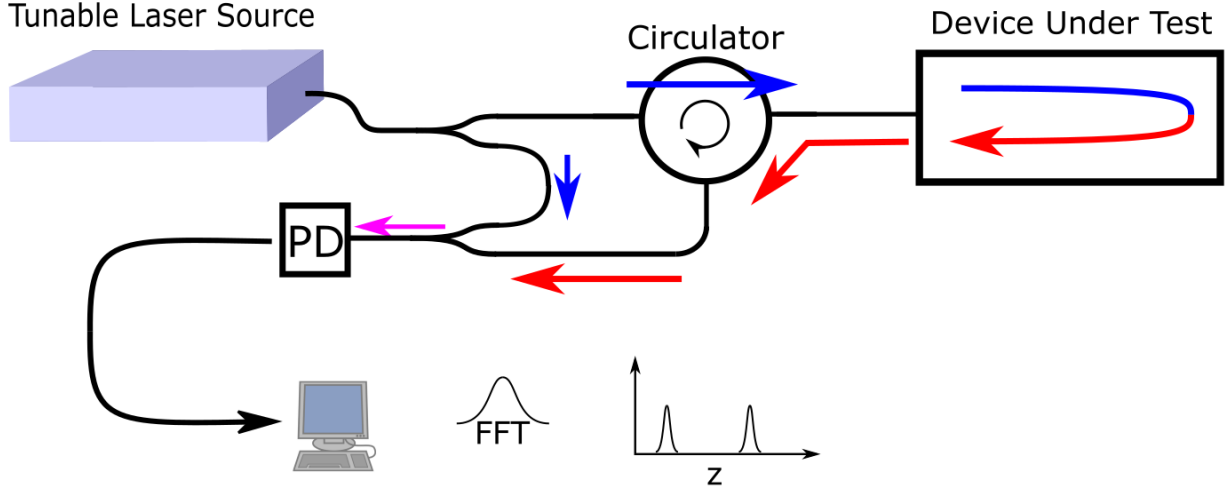


Figure 1.2: A diagram of an OFDR implementation. Light from a wavelength-swept tunable laser source enters a coupler and is split to a path going to the device under test (DUT) and a path going to the photodetector (PD) as the local oscillator. The light going to the DUT passes through a circulator, and the reflection from the DUT enters the circulator and is directed to the PD. The local oscillator and reflection are mixed at the PD using a second 2×2 coupler. A fast Fourier transform (FFT) is performed on the electrical output of the PD. The positions of reflection sites are deduced from the FFT.

As the frequency (f) of the tunable laser source is swept at a rate γ , starting from frequency f_0 , [26] the instantaneous laser frequency ($f(t)$) is given by

$$f(t) = f_0 + \gamma t. \quad (1.1)$$

The electric field of the LO (denoted as E_{LO}) and the reflections from the DUT (denoted as E_{DUT}) are respectively,

$$E_{LO}(t) = E_0 \exp(j(2\pi f_0 t + \pi \gamma t^2)), \quad (1.2)$$

$$E_{DUT}(t) = \sqrt{R(\tau)} E_0 \exp(j(2\pi f_0(t - \tau) + \pi \gamma(t - \tau)^2)),$$

where τ is the temporal delay between the LO and the reflections coming back from the DUT.

Interfering the two signals in (1.2) yields the expression for the photodetector current, $I(t)$,

$$I(t) \propto |E_{LO}(t) + E_{DUT}(t)|^2 = E_0^2 + R(\tau)E_0^2 + 2\sqrt{R(\tau)}E_0^2 \cos\left(2\pi\left(f_0\tau + \gamma\tau t + \frac{1}{2}\gamma\tau^2\right)\right). \quad (1.3)$$

The beating frequency term, $f_{beat} = \gamma\tau/2\pi$, with the accompanying $R(\tau)$ amplitude term can then be extracted by performing a Fourier transform on the measured interferogram. The beating frequency term f_{beat} extracted by the Fourier transform, is related to the spatial location of the reflection by the following relationship, assuming zero group velocity dispersion,

$$z = \frac{f_{beat}c\pi}{\gamma n_{DUT}}, \quad (1.4)$$

where n_{DUT} is the group index of the DUT. And the intensity of the beating frequency is proportional to the intensity of the reflection at that location through the following relation,

$$\frac{2}{N}|F(z)| = R(z), \quad (1.5)$$

where F is the Fourier transform of the time series signal and N is the number of sample points in the time series signal.

1.2 Polarization Diverse OFDR

To enable a polarization distinguishing OFDR measurement for a photonic OFDR implementation, an external polarization can be used to introduce a polarization dependent delay between the photonic chip and the DUT. This passive external polarization management shifts the beating frequency of the various components of the Jones matrix, sacrificing maximum detection range for a polarization diverse measurement. An example of this is shown in Figure 1.3.

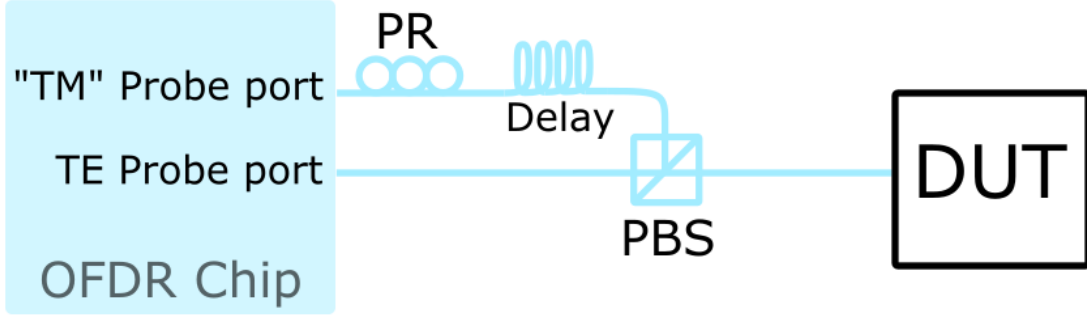


Figure 1.3: A diagram of external polarization management assembly; the TE polarized light coming from the “TM” probe port under goes polarization rotation (PR) into the orthogonal polarization, and a temporal delay τ is applied through a delay line, and combined with the TE polarized light from the TE probe port in the polarization beam splitter (PBS) and sent to the device under test (DUT), resulting in the TM polarized light in the combined beam containing a temporal delay τ relative to the TE polarized light. The 2 polarizations in the back reflections from the DUT is split by the PBS, with the TM component acquiring an additional delay τ before it reenters the OFDR chip. The TM \rightarrow TM and TE \rightarrow TM reflections will be collected at the “TM” probe port with an applied temporal delay of 2τ and τ respectively. The TE \rightarrow TE and TM \rightarrow TE reflections will be collected at the TE probe port with an applied temporal delay of 0 and τ respectively. The difference in temporal delays translate to a spatial offset after the interference is Fourier transformed, multiplexing the terms of the reflection’s Jones matrix spatially.

Alternatively, polarization management can also be integrated with the photonic OFDR chip by utilizing polarization splitters or polarization splitter rotators. [27], [28]

Following from the Fast Fourier transform step involved for determining the spatial location and intensity of the reflections in the DUT, several limitations on the OFDR implementation can be derived from properties of the Discrete Fourier Transform (DFT).

1.3 Spatial Resolution

The relationship between the width of frequency bins to the sample time for DFT is given as,

$$\Delta f = \frac{1}{T_{sample}}, \quad (1.6)$$

where Δf is the width of a frequency bin, T_{sample} is the total sampling time. The corresponding relationship in the context of OFDR relates the spatial detection resolution to the range of the tunable laser source (TLS) frequency sweep, assuming zero GVD, is given as

$$\Delta z = \frac{c}{2n_{DUT}\Delta f_{TLS}}, \quad (1.7)[25]$$

where Δf_{TLS} is the frequency range of the TLS, n_{DUT} is the group index of the device under test. This shows an inverse relationship between the minimum distinguishable feature size and the range of the TLS frequency sweep used in the OFDR technique.

1.4 Maximum range

From the Nyquist theorem, which relates the time series sampling frequency to the maximum frequency extracted from the signal (f_{max}), the maximum frequency that can be measured from a time series. $f_{nyquist}$, is given by

$$f_{nyquist} = \frac{1}{\Delta t}, f_{max} \leq f_{nyquist}/2 \quad (1.8)$$

where Δt is the time step of the time series data. The corresponding relationship in the context of OFDR relates the maximum range, z_{max} , to the frequency resolution of the TLS sweep is given as,

$$z_{max} = \frac{c}{4n_g(DUT)\Delta f} \quad (1.9)$$

where Δf is the frequency resolution of the TLS sweep, constrained by either the linewidth of the TLS or the sampling frequency of the TLS sweep.

While the limitations on the linewidth, sweep speed and sampling frequency of the TLS is outside of the scope of this thesis, the target spectral bandwidth of the photonic circuit will constrain the spatial resolution of the OFDR system.

1.5 Role of 2×2 couplers

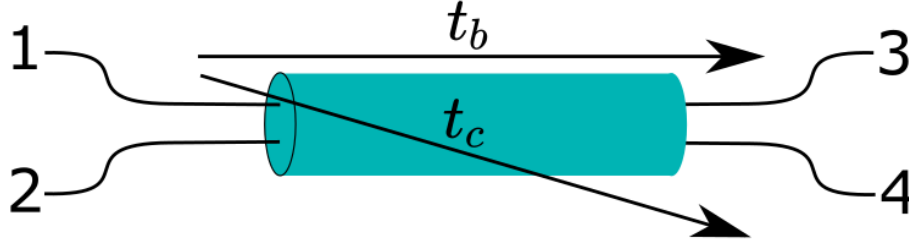


Figure 1.4: A diagram of a 2×2 coupler. t_b , t_c are the bar and cross port coupling coefficient, respectively

A critical device in the operation of OFDR is the 2×2 coupler. On a photonics platform without non-reciprocal properties, the 2×2 coupler acts both as the circulator, in which the reflections coming back from the DUT is redirected towards the interferometer, as well as the interferometer itself, in the form of a coherent detector in a balanced configuration.

1.5.1 Balanced Detection

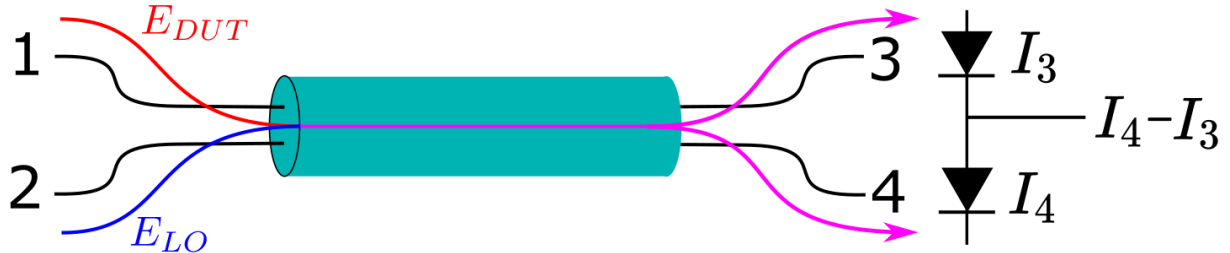


Figure 1.5: A diagram showing balanced photodetection. E_{DUT} is the back reflection from the device under test (DUT), E_{LO} is the local oscillator (LO). The outputs at port 3 and 4 are incident on photodetectors generating a photocurrent of I_3 and I_4 . The output of the balanced detection is the difference between the photocurrents I_3 and I_4

One of the major advantage of coherent OFDR techniques is the enhanced sensitivity, owing in large part due to the capability for a coherent balanced detector to suppress relative intensity noise originating from the TLS. [19], [29]

Balanced detection involves the mixture of two input signals incident on port 1 and 2 in a 2×2 coupler as shown in Figure 1.5, using the expressions for E_{LO} and E_{DUT} from (1.2), the detected photocurrents at output ports 3 and 4, I_3 and I_4 , respectively are

$$I_3 \propto |t_b E_{DUT} + t_c E_{LO}|^2 = |t_c|^2 E_0^2 + |t_b|^2 R(\tau) E_0^2 + 2\sqrt{R(\tau)} E_0^2 |t_b t_c| \cos\left(2\pi\left(f_0\tau + \gamma\tau t + \frac{1}{2}\gamma\tau^2\right) + \phi\right), \quad (1.10)$$

$$I_4 \propto |t_c E_{DUT} + t_b E_{LO}|^2 = |t_b|^2 E_0^2 + |t_c|^2 R(\tau) E_0^2 - 2\sqrt{R(\tau)} E_0^2 |t_b t_c| \cos\left(2\pi\left(f_0\tau + \gamma\tau t + \frac{1}{2}\gamma\tau^2\right) + \phi\right),$$

where t_b and t_c are the bar and cross port coupling coefficients and ϕ is the differential phase accumulated between the bar and cross ports. By taking the difference between photodetector currents, we obtain

$$I_4 - I_3 = (|t_b|^2 - |t_c|^2) E_0^2 + (|t_c|^2 - |t_b|^2) R(\tau) E_0^2 + 4|t_b t_c| \sqrt{R(\tau)} E_0^2 \cos\left(2\pi\left(f_0\tau + \gamma\tau t + \frac{1}{2}\gamma\tau^2\right) + \phi\right). \quad (1.11)$$

If the bar and cross coupling coefficients of the 2×2 coupler are perfectly balanced, the DC terms E_0^2 and $R(\tau) E_0^2$, and the relative intensity noise associated with those terms are completely eliminated while the signal of interest is doubled. [29], [30]

1.5.2 Reflection Isolation

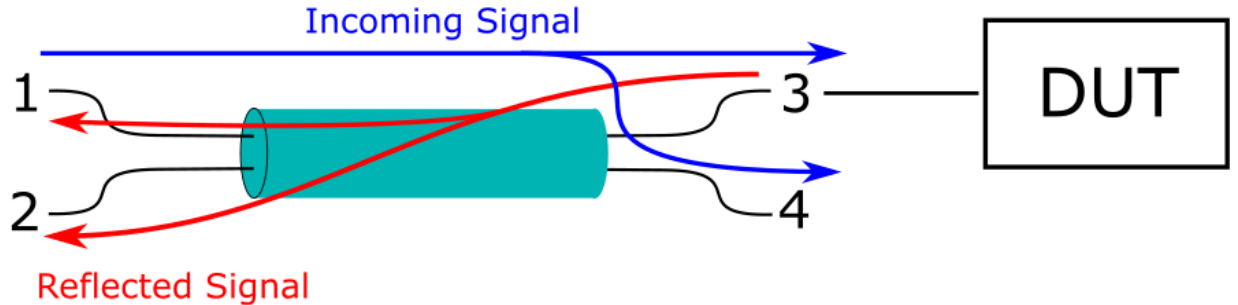


Figure 1.6: A diagram of 2×2 coupler acting as a circulator. The incoming signal from the tunable laser source enters through port 1 and is routed to ports 3 and 4. Port 3 is connected to the device under test (DUT). Back reflections from the DUT enter through port 3 and is routed to ports 1 and 2. Back reflections are isolated in port 2.

On the SiN-on-Si platform, the lack of materials exhibiting non-reciprocal properties means an optical circulator cannot be integrated as a part of the photonic circuit. Instead, the 2×2 coupler can be used to separate the reflected signal into a port different from the input port. Figure 1.5 shows the process: incident light is launched from Port 1 and the output emerges in Ports 3 and 4. A reflection in Port 3 from the DUT is directed into Port 2 and Port 1; thus, the reflection can be

characterized in Port 2. This incurs at least a 6 dB excess loss compared to an optical circulator, some of which can be salvaged by using the light from port 4 as the LO for the interferometer.

1.6 Thesis Outline

This thesis will place an emphasis on the exploration and design of a broadband 2×2 coupler optimized for the functions of isolating back reflections from the DUT and facilitating balanced detection for the realization of an integrated optics implementation of OFDR. In Chapter 2, the SiN-on-Si photonic platform will be defined and the basic devices that enable photonic circuits will be detailed and designed. An outline of an integrated OFDR implementation will also be presented. In Chapter 3, the performance of 2×2 couplers in the roles of isolating reflections and facilitating balanced detection will be parameterized and the design and simulation of multiple types of 2×2 couplers will be optimized and evaluated for those parameters. In Chapter 4, the test structures designed for the purpose of characterizing the general devices and optimized 2×2 couplers, as well as the measurement setup and methodologies will be detailed. In Chapter 5, the measurement results for the various test structures will be provided, and device performances will be extracted from the measurement results. In Chapter 6, the conclusions of this thesis will be summarized, and offer some future outlooks for this work.

Chapter 2

SiN-on-Si Photonic Platform

This chapter will introduce the SiN-on-Si foundry processed platform on which the integrated OFDR system is proposed and the 2×2 couplers have been fabricated and tested. The strip waveguide dimensions will be chosen. Then the need for, the design, and simulation results of general components in the SiN-on-Si platform, such as interlayer transitions, edge couplers, polarization filters and Ge photodetectors, will be briefly reviewed. This chapter concludes with an overview on how the OFDR system would be implemented on the SiN-on-Si platform in terms of the above building blocks in addition to the 2×2 couplers to be designed in Chapter 3.

2.1 SiN-on-Si Platform

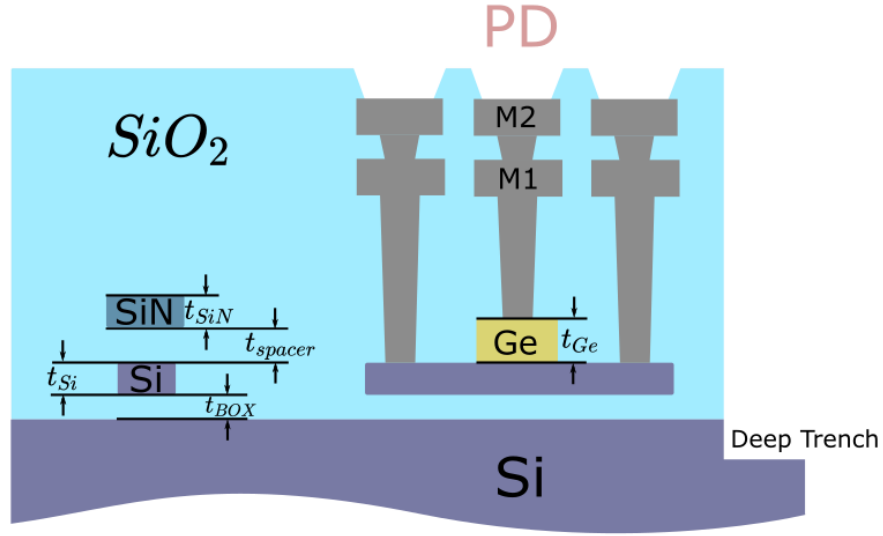


Figure 2.1: Cross-section of the multi-layer SiN-on-Si platform used in this work (not to scale). $t_{Si} = 150nm$, $t_{SiN} = 400nm$, $t_{spacer} = 200nm$, $t_{BOX} = 2\mu m$, $t_{Ge} = 500nm$

The devices are fabricated on a SiN-on-Si platform provided from the former Institute of Microelectronics (IME A*Star), now Advanced Micro Foundry (AMF). The Si photonic layer is defined by partial or complete etching of top layer Si of the SOI wafer for strip or rib waveguides. Additional layers on the platform are deposited on top of the SOI wafer through a series of deposition, etching and planarization steps. [12] The platform is similar to the platform described in [12], [31] with a photonic Si_xN_y layer 400nm thick deposited through the PECVD process. PECVD is chosen for its compatibility with ion implantation processes, and therefore the optoelectronic capabilities in the platform, owing to the lower deposition temperature compared to the LCPVD process.[12] However, since PECVD SiN is not stoichiometric, a wider range of refractive indices can be potentially realized compared to LPCVD, which results in stoichiometric Si_3N_4 . [32] Metal vias connect the active optoelectronics of the platform to the metal (Aluminum) routing layers M1, and M2, which can be opened as a bond pad. TiN heaters are also available on this platform but was not utilized.

This platform leverages the lower waveguide dispersion of SiN for broadband passive devices while retaining access to the optoelectronic capabilities of Si, specifically the Ge photodetectors for the proposed integrated OFDR system.

2.2 Waveguide dimensions

A waveguide width sweep was performed for SiN and Si strip waveguides in Lumerical MODE solutions and the effective indices for various waveguide modes are shown in Figure 2.2.

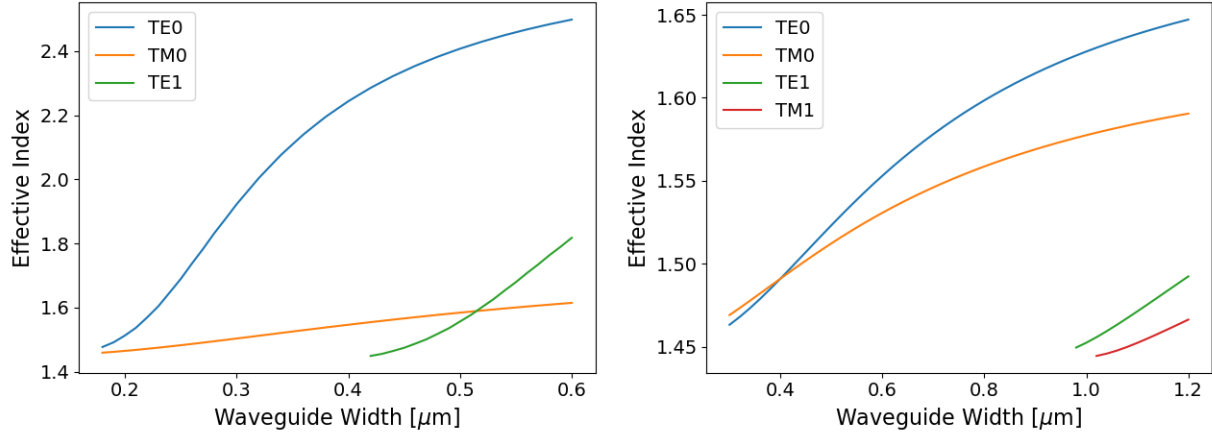


Figure 2.2: Effective index of supported waveguide modes at 1310nm, Si strip waveguide with a height of 220nm and refractive index of 3.507 (left) and SiN strip waveguide with a height of 400nm and refractive index of 1.905 (right)

The nominal SiN strip waveguide width was chosen to be 750nm to ensure single mode propagation in the entirety of the targeted wavelength range taking into consideration the potential fabrication variations in the refractive index, width, and thickness of the waveguides.

Similarly, the silicon waveguide width was chosen to be 350nm for single mode operation in the target wavelength range, taking into consideration the potential width and thickness variations.

2.2.1 Polarizer

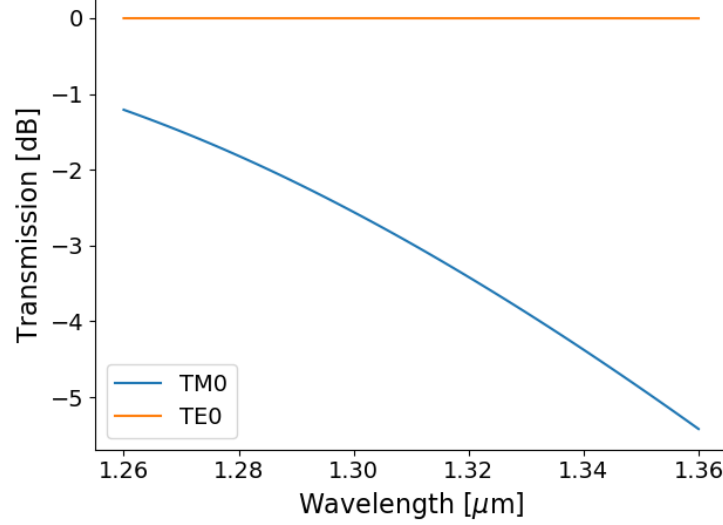


Figure 2.3: The simulated transmission of TE0 and TM0 modes in a Si strip waveguide with a height of 220nm and width of 350nm through a 90° bend with a radius of 10μm

Due to the poor lateral confinement of the TM0 mode on the Si waveguide dimensions chosen in Section 2.2, tight bends leads to a large polarization dependent loss (PDL) in favor of the TE0 mode. Tight bends with radii of 10μm were used to filter out the unwanted TM0 mode. The losses incurred in a 90° bend is shown in Figure 2.3 with >1dB PDL for TM0 and negligible losses for TE0 between 1.26μm and 1.36μm, The combination of better mode confinement, high edge-coupling efficiency, and the ability to selective filter out TM0 makes TE0 the desired mode for operation.

2.3 General Devices

In the following sections, brief descriptions of several devices on the SiN-on-Si platform needed for the OFDR implementation are given, as well as their expected performances through simulations in Lumerical MODE and Finite-difference Time-domain (FDTD) software.

2.3.1 Edge coupler

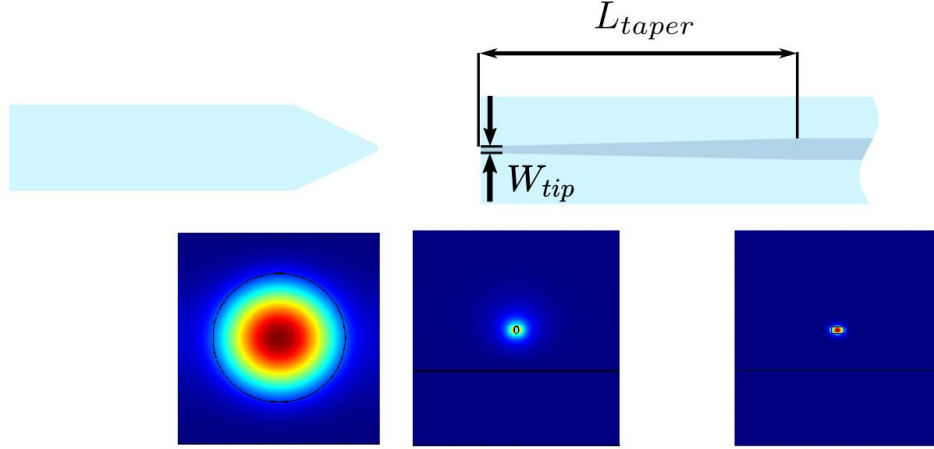


Figure 2.4: The geometric definition of the inverse spot size converter and the simulated TE_0 mode profile at various points along the device. W_{tip} is the width of the tip, L_{taper} is the length of the linear taper from the tip width to the nominal waveguide widths of SiN (750nm) and Si (350nm).

To efficiently couple light onto and off the chip, inverse taper spot size converters are utilized to minimize the mode mismatch between the fibre and the waveguides on chip. [33], [34] The power overlap of the mode of an SMF28 fibre and the inverse taper is calculated in the Lumerical MODE software and is tabulated in Table 2.1 [35].

Table 2.1: Table of power coupling between SMF28 fibre mode and minimum dimensions on SiN (200nm) and Si (180nm)

	TE0	TM0
SMF28 \rightarrow SiN	0.71	0.5
SMF28 \rightarrow Si	0.17	0.305

The edge couplers are defined in the SiN layer since the mode overlap between the fibre and inverse taper is significantly higher due to the larger spacing between the SiN photonic layer and the Si substrate compared to the Si photonic layer. The edge coupler designed for this thesis linearly widens from the minimum allowable waveguide width on the SiN layer to the strip waveguide width defined

in Section 2.2. The linear taper length (L_{taper}), as defined in Figure 2.4, is swept with the Eigenmode Expansion (EME) solver in the Lumerical MODE software with the TE0 mode, then its spectral characteristics is obtained through a perturbative wavelength sweep. The results are shown in Figure 2.5, which illustrates that a taper with a length of $>500\mu m$ is sufficient for $>90\%$ transmission and that the coupling efficiency has $<10\%$ variation across the wavelength band ranging from $1.26\mu m$ to $1.36\mu m$.

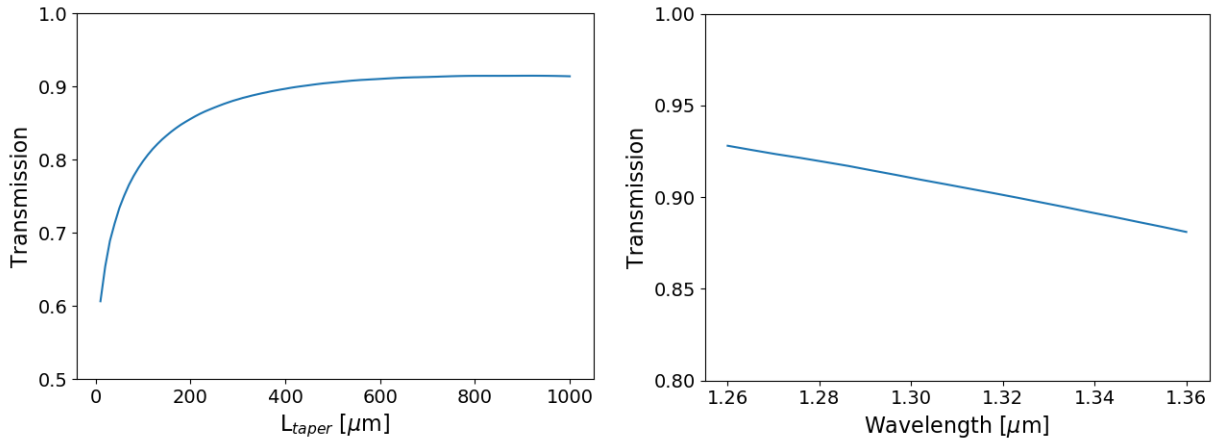


Figure 2.5: (left) The L_{taper} sweep results for the TE0 mode transmission for the SiN inverse taper at 1310nm. (right) The wavelength sweep for TE0 mode transmission for the SiN inverse taper with $L_{taper} = 500\mu m$.

In finding a good trade-off between coupling efficiency and device footprint, an inverse taper length of $500\mu m$ was chosen for the inverted spot size converter.

2.3.2 Interlayer Transitions

Having two photonic layers on the platform necessitates the efficient transfer of light between the two layers, which in this case, the transfer of light from the SiN layer to the Si layer for detection by the Ge photodetector. To achieve a low loss and broadband interlayer transition, an adiabatic linear taper is utilized, where the waveguides on both SiN and Si layer are tapered to facilitate an adiabatic evolution from the propagating mode on one photonic layer to the other. [12], [36]–[38]

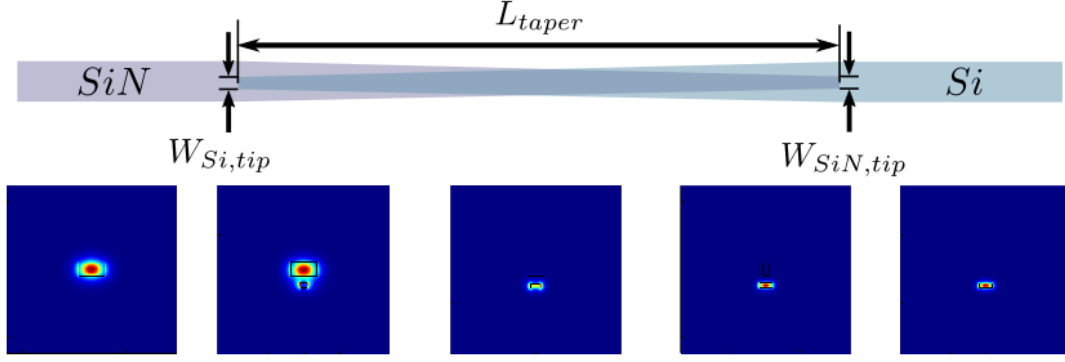


Figure 2.6: The geometric definition for interlayer transition between the SiN and Si layers and the simulated TE0 mode profile at various points along the device. $W_{Si,tip}$ and $W_{SiN,tip}$ are the tip widths of the Si and SiN tapers respectively, and L_{taper} is the length of the linear taper in the interlayer transition.

The adiabatic transition is defined as two linear tapers with blunt tip widths $W_{Si,tip}$ and $W_{SiN,tip}$ constrained by the minimum feature sizes dictated by the design rules for each layer respectively, which tapers up to the strip waveguide widths defined in Section 2.2. By minimizing the blunt tip widths, the initial perturbation to the propagating mode is minimized and the reflection at the transition is reduced. [12]

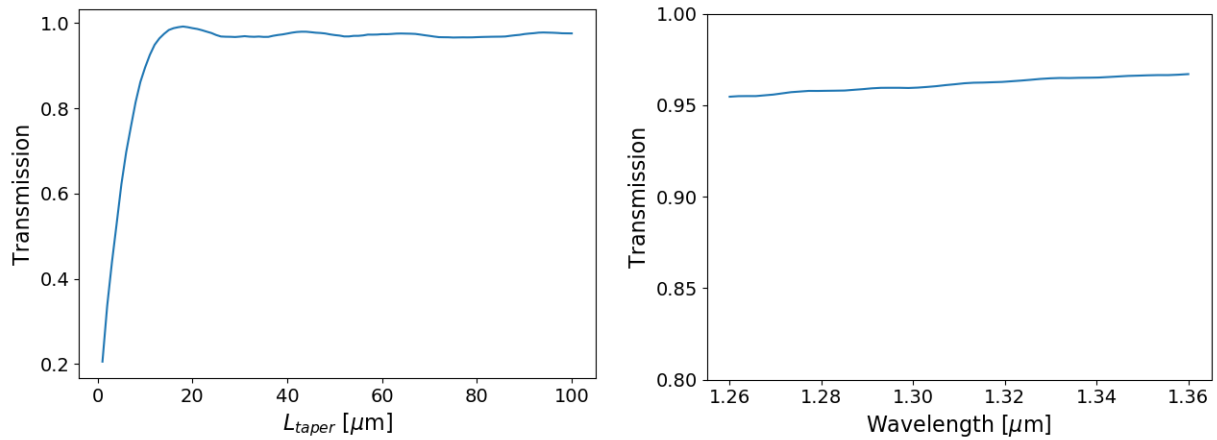


Figure 2.7: (left) L_{taper} sweep results for the TE0 mode transmission of the interlayer transition. (right) FDTD simulation results for the TE0 mode transmission of the interlayer transition with $L_{taper} = 100 \mu m$

The interlayer transition taper length (L_{taper}) was swept in the EME solver in Lumerical MODE software. Figure 2.7 demonstrates that a L_{taper} of $100 \mu m$ results in a $>95\%$ transmission in the

interlayer transition in between $1.26\mu\text{m}$ and $1.36\mu\text{m}$. L_{taper} is chosen to be $100\mu\text{m}$ to be fully ensure the transition is adiabatic.

2.3.3 Ge Photodetector

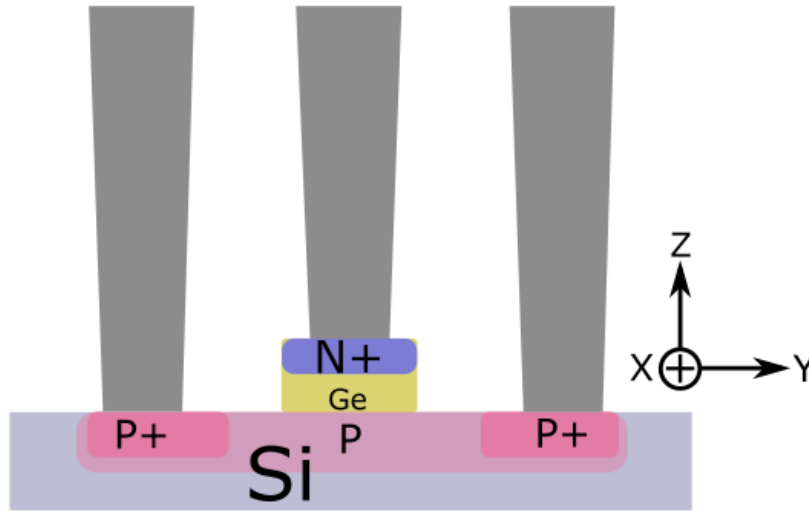


Figure 2.8: Cross-sectional view of the Ge Photodetector. The silicon (Si) and germanium (Ge) are P and N doped respectively to form a P-I-N junction. P+ and N+ doping are used create ohmic contacts with the metal.

The photodetector (PD) on the chip is a vertical P-I-N junction similar to the vertical photodetector described in [11], [39]. The P-I-N junction is formed between the P-doped Si photonic layer and the N-doped Ge which is epitaxially grown on top of the Si layer. The light propagating in Si slab is coupled evanescently into the Ge, generating carriers which are swept up by the electric fields in the depletion region. The N+ and P+ doping on the Ge and Si layers respectively form the ohmic metal contacts with the vias which connect to the metal routing layers M1 and M2.

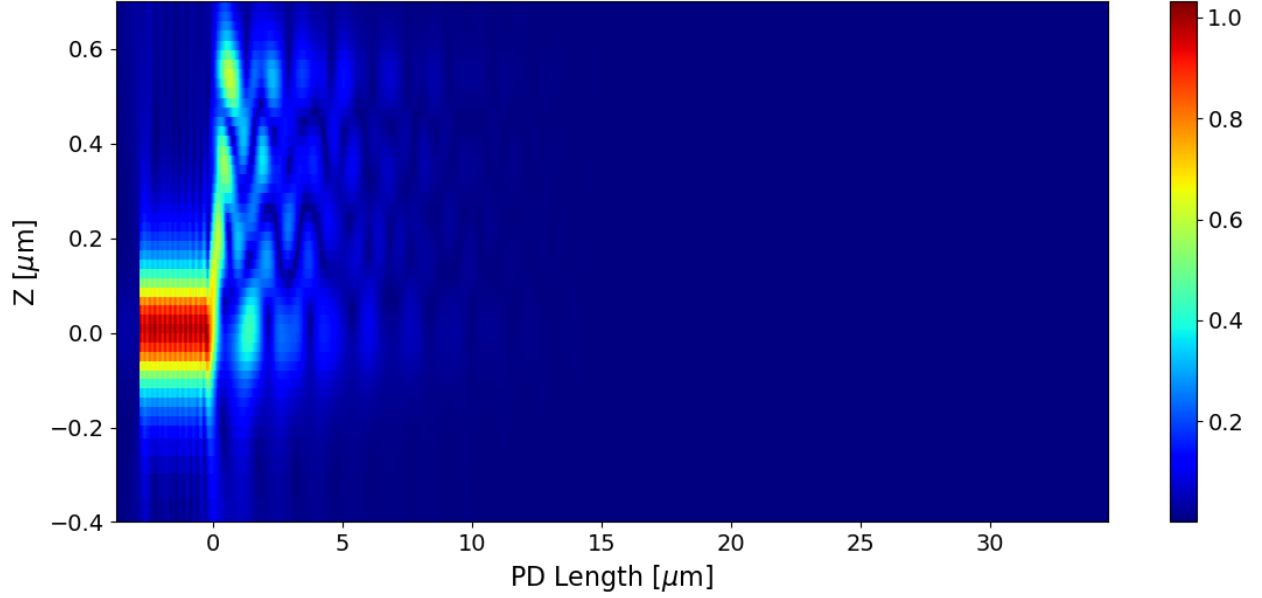


Figure 2.9: The electric field intensity profile inside the Ge photodetector as simulated by the FDTD method.

FDTD simulation result seen in Figure 2.9 is used to ensure that the PD length of $>15\mu\text{m}$ is sufficiently long to absorb the majority of the incoming light in the Ge. The design of the Ge PD is standard in the foundry, which has a PD length of $50\mu\text{m}$ which should be sufficiently long to effectively absorb all the incoming light.

2.4 Photonic OFDR System Overview

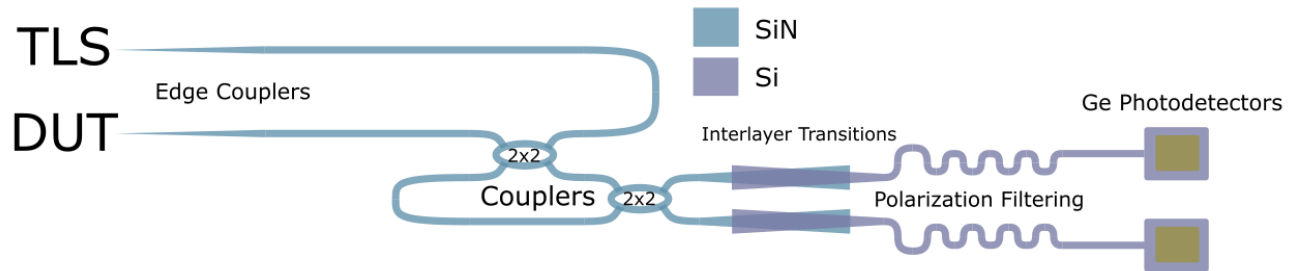


Figure 2.10: A schematic of OFDR implementation on a SiN-on-Si platform using edge couplers, interlayer transitions, polarization filters, photodetectors and 2×2 couplers. The light from the tunable laser source (TLS) is coupled into the SiN layer through the edge couplers, goes towards the 2×2 coupler, and is split into the device under test (DUT) and the local oscillator (LO). The back reflected signal from the DUT combines with the LO in the second 2×2 coupler, and the mixed signals are transited down through interlayer transitions to the Si layer, where it undergoes polarization filtering, and is detected by the Ge photodetectors.

A proposed OFDR implementation on SiN-on-Si platform is shown in Figure 2.10. The TLS input coupled into the SiN photonic layer by the inverse spot-size converter as defined in Section 2.3.1, split into a reference and probe arm through a 2×2 coupler, coupled out, and the back reflection is interfered with the reference in a balanced detection configuration before the light is transferred to the Si photonic layer through the adiabatic interlayer transition as defined in Section 2.3.2, filtered for TM polarized modes through a series of tight bends as defined in Section 2.2.1, and subsequently detected with the Ge PD as defined in Section 2.3.3 to measure the interferogram and subsequently calculate the location and intensities of reflections in the DUT as detailed in the Chapter 1.

2.5 Summary

In this chapter, the SiN-on-Si platform and various devices needed for general operation and the photonic implementation of OFDR are described. Devices such as the inverted spot-size converter, interlayer transition, TM polarization filter, and Ge PD are designed and simulated to obtain expected performance on our SiN-on-Si platform. A proposed architecture for a basic and polarization diverse OFDR implementation on a SiN-on-Si platform are described.

Chapter 3

2×2 Couplers Theory and Design

2×2 couplers that equally divide input fields from each input port into two output ports are important devices in integrated photonics and forms the basic building block for many devices ranging from optical switches, modulators, and filters. [40]–[42] In the application of an integrated optic OFDR implementation, 2×2 couplers are needed to isolate the back reflection from the DUT and facilitate the interference between the LO and the back reflection from the DUT. For OFDR applications, besides having low loss, it is important for the 2×2 couplers to be as broadband as possible to achieve a high spatial resolution. In this chapter, the theory, design, and optimization of different types of 2×2 couplers for those functions will be presented. We will begin with the parameterization of the 2×2 coupler performance as it relates to their roles in the proposed integrated OFDR system. Then, the theories of various types of 2×2 couplers are presented, followed by their design and optimization through a combination of design techniques and simulation in Lumerical MODE and FDTD software. This chapter will conclude with the comparison and scoring of the optimized designs for different implementations of the 2×2 coupler in their roles in the OFDR implementation.

3.1 Design Goals

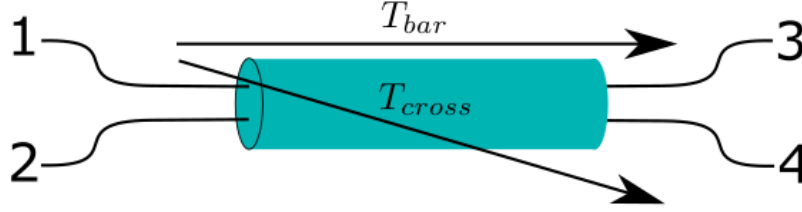


Figure 3.1: Schematic overview of 2×2 coupler. T_{bar}, T_{cross} are the bar and cross port transmissions respectively

One of the roles of the 2×2 coupler on a photonic platform without non-reciprocal optical properties is to replicate the function of a circulator to redirect and isolate back reflections coming from the DUT. However, the drawback of utilizing a 2×2 coupler instead of a circulator for this purpose is the excess loss incurred when the light is transmitted from Port 1 to Port 3 and the reflection from Port 3 is transmitted to Port 2. To evaluate device performance for isolating back reflections from the DUT, the back reflected power relative to the input is parameterized as T_{refl} and is given by

$$T_{refl} = 10 \times \log_{10}(T_{cross}T_{bar}), \quad (3.1)$$

where T_{cross} is the transmission in the cross port and T_{bar} is the transmission in the bar port. When T_{refl} is maximized, the loss is minimized. Since T_{cross} and T_{bar} are competing factors, T_{refl} is maximized when the outputs are balanced ($T_{cross} = T_{bar}$), with any insertion losses incurring additional penalties.

To facilitate the interference between the LO and the back reflected signal from the DUT in a balanced detector configuration, the DC signal rejection is proportional to the balance of the output ports. We define the Single Port Rejection Ratio (SPRR) as a metric of the 2×2 coupler performance for balanced photodetection. The SPRR is the relative intensity of the interference fringes compared to the suppressed DC signal, which is given as [30]

$$SPRR = 10 \times \log_{10} \frac{4\sqrt{T_{cross}T_{bar}}}{|T_{bar} - T_{cross}|}. \quad (3.2)$$

SPRR is similarly maximized when the outputs are balanced and insertion losses are low, but SPRR is heavily weighted towards the balance of the outputs.

As previously mentioned, the minimum distinguishable spatial feature of OFDR is inversely proportional to the frequency sweep range of the OFDR technique.[43] For this reason, each of the 2×2 coupler candidates will be evaluated for the worst case SPRR and T_{refl} within the targeted wavelengths ranging from $1.26\mu m$ to $1.36\mu m$. Due to variations in the foundry fabrication processes, the couplers will also be evaluated for tolerance against fabrication variations such as over/under etching, height variations, and index deviations from the provided refractive index. Additionally, due to the sensitivity of OFDR systems to reflections within the system, which can cause second order phantom reflections through either interference with the LO, or with real reflections coming from the DUT, the reflection of the 2×2 coupler should also be minimized. [19] To summarize, for isolating the back reflection from the DUT and mixing the LO and back reflected signals in the OFDR implementation, the ideal 2×2 coupler should exhibit a balanced output with minimal insertion loss and reflections across the targeted wavelength range of the OFDR system, with resilience to fabrication variations.

3.2 Comparison of 2×2 couplers

There are multiple devices which can fulfill the role of a 2×2 coupler, including directional couplers, multimode interferometer (MMI) couplers, and adiabatic couplers. This section will detail the theory behind each of those devices, followed by the design and optimization of each for its role in photonic implementation of OFDR.

3.2.1 Multimode Interferometer (MMI)

Multimode interferometers operate by introducing the guided light to a large slab region, in which the guided light is decomposed into multiple supported guided modes which propagate and interfere to form images at varying distances along the slab. [44]

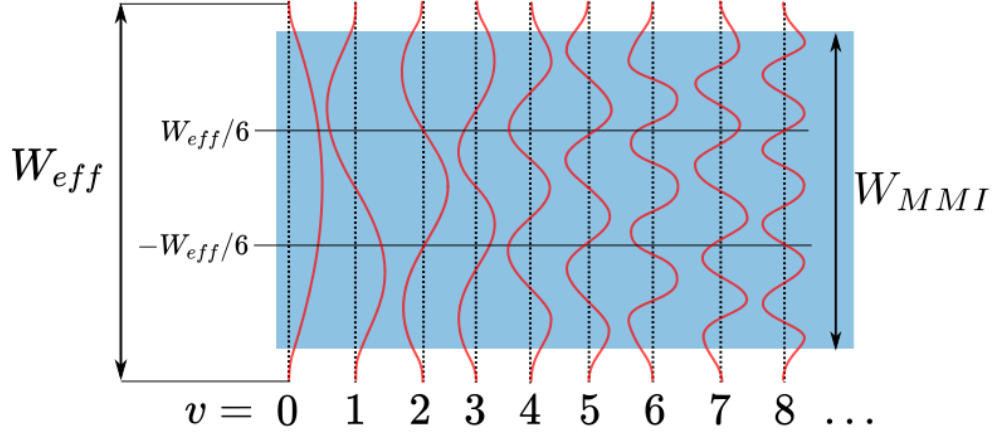


Figure 3.2: A diagram of slab modes in slab region of the MMI recreated from [44]. W_{eff} is the effective width of the slab modes, and W_{MMI} is the width of the slab region.

The dispersion relation of the multimodal region can be approximated through Effective Index Model as

$$k_{yv}^2 + \beta_v^2 = k_0^2 n_r^2: k_0 = \frac{2\pi}{\lambda_0}, \quad k_{yv} = \frac{(v+1)\pi}{W_{ev}}. \quad (3.3)[44]$$

Where v is the mode number, k_0 is the free space propagation constant, λ_0 is the wavelength, n_r is the index of the slab region, W_{ev} is the penetration depth of the v -th mode. For simplicity W_{ev} is approximated as W_{eff} .

The waveguide propagation constant for the v -th mode by applying binomial approximation given

$k_{yv} \ll k_0 n_r$ is

$$\beta_v = k_0 n_r - \frac{(v+1)^2 \pi \lambda_0}{4 n_r W_{eff}^2}. \quad (3.4)[44]$$

The input image $\Psi(y, 0)$ is decomposed in terms of the guided modes $\psi_v(y)$,

$$\Psi(y, 0) = \sum_{v=0}^{m-1} c_v \psi_v(y), \quad (3.5)[44]$$

here c_v is the coupling coefficient from the input image to the v -th guided mode. This is generalized to the following as the field propagates along z :

$$\Psi(y, z) = \sum_{v=0}^{m-1} c_v \psi_v(y) \exp[j(\beta_0 - \beta_v)z] = \sum_{v=0}^{m-1} c_v \psi_v(y) \exp\left[j \frac{v(v+2)\pi}{3L_\pi} z\right], \quad (3.6)$$

$$L_\pi = \frac{4n_r W_e^2}{3\lambda_0},$$

where L_π is the beat length of the two lowest order modes [44]. As the guided slab modes propagate, they come in and out of phase and eventually reconstruct the input image $\Psi(y, 0)$ at $z = 3L_\pi$. At $z = 3L_\pi/2$, (3.6) becomes [44]

$$\Psi\left(y, \frac{3}{2}L_\pi\right) = \sum_{v \text{ even}} c_v \psi_v(y) + \sum_{v \text{ odd}} -j c_v \psi_v(y) = \frac{1-j}{2} \Psi(y, 0) + \frac{1+j}{2} \Psi(-y, 0). \quad (3.7)$$

which produces a two-fold image symmetrically about the center of the slab, which fulfills the function of a 2×2 coupler.

The optical bandwidth of a MMI coupler is inversely proportional to the two-fold image length of the slab region.[45] To improve the optical bandwidth, the length of the mode beating region can be further reduced by utilizing restricted interference, in which select modes are deliberately not excited to reduce the beat length of the MMI.[44]

Furthermore, we note that

$$\text{mod}_3(v(v+2)) = 0, \text{ for } v \neq 2, 5, 8 \dots \quad (3.8)$$

Combining (3.8) with (3.6), results in the length required for the condition (3.7) is reduced by a factor of 3 to $L_\pi/2$ if the slab modes $v = 2, 5, 8, \dots$ are not excited. This restricted interference can be achieved by positioning the waveguide inputs at $\pm W_{eff}/6$ about the center of the slab, where the nulls of the slab modes $v = 2, 5, 8, \dots$ are located and are therefore minimally excited as shown in Figure 3.2.

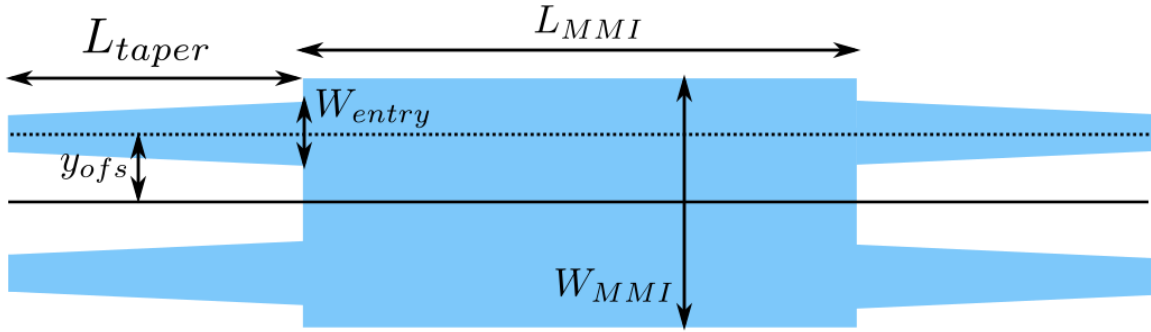


Figure 3.3: The geometric definition of proposed multimode interferometer (MMI). L_{MMI} and W_{MMI} are the length and width of the slab region of the MMI. L_{taper} is the taper length of the entry and exit waveguides from the nominal waveguide widths to the entry waveguide width (W_{entry}). y_{ofs} is the centerline offset between entry and exit waveguides and the center of the slab region.

The geometric definition of the MMI coupler is shown in Figure 3.3. Initial parameter exploration was done in mode solver and eigenmode expansion in Lumerical MODE software by placing the input waveguides at a offset (y_{ofs}) of $W_{eff}/6$ and sweeping the width (W_{MMI}), effective width (W_{eff}) while optimizing the length of the MMI slab regions. Spectral characteristics are obtained through wavelength perturbation sweeps in the eigenmode expansion results.

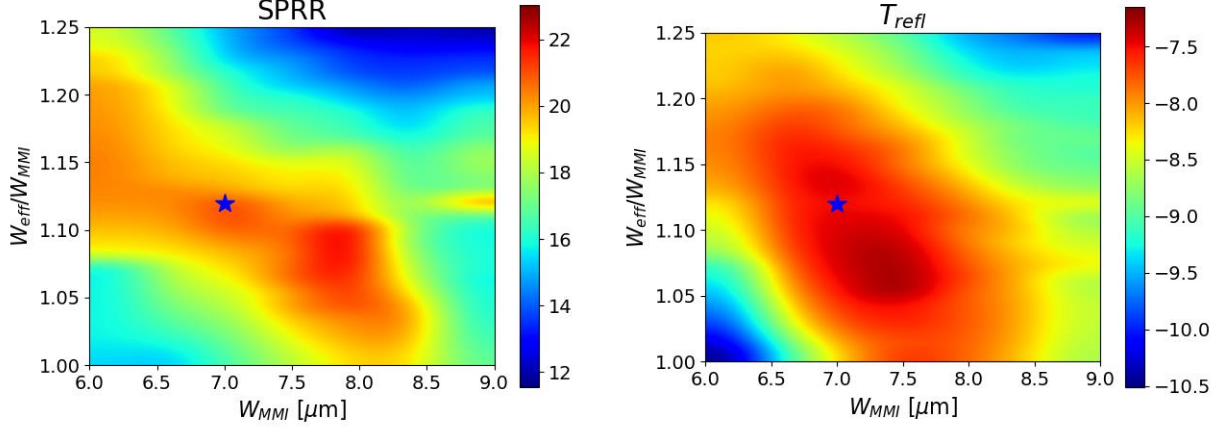


Figure 3.4: Initial parameters W_{MMI} , W_{eff}/W_{MMI} sweep in EME solver for calculated worst case single port rejection ratio (SPRR, left), and T_{refl} (right) in the target wavelength range (1260-1360nm) Star denotes the initial parameters for MMI design.

A suitable tradeoff between performance in both roles is found with the parameters $W_{MMI} = 7 \mu m$, $W_{eff}/W_{MMI} = 1.12$, which are taken as the initial parameters for the MMI design. The initial guess was optimized by tuning the MMI length (L_{MMI}), input waveguide width (W_{entry}) and displacement (y_{ofs}) in FDTD. The final optimized parameters are summarized in Table 3.1.

Table 3.1: Table of MMI parameters, for the initial guess and the optimized design

Parameters	Initial Guess	Optimized Final Design
$W_{MMI} [\mu m]$	7.0	7.0
$L_{MMI} [\mu m]$	57.6	56.9
$y_{ofs} [\mu m]$	1.318	1.4
$W_{entry} [\mu m]$	1.76	1.81
$L_{taper} [\mu m]$	---	10

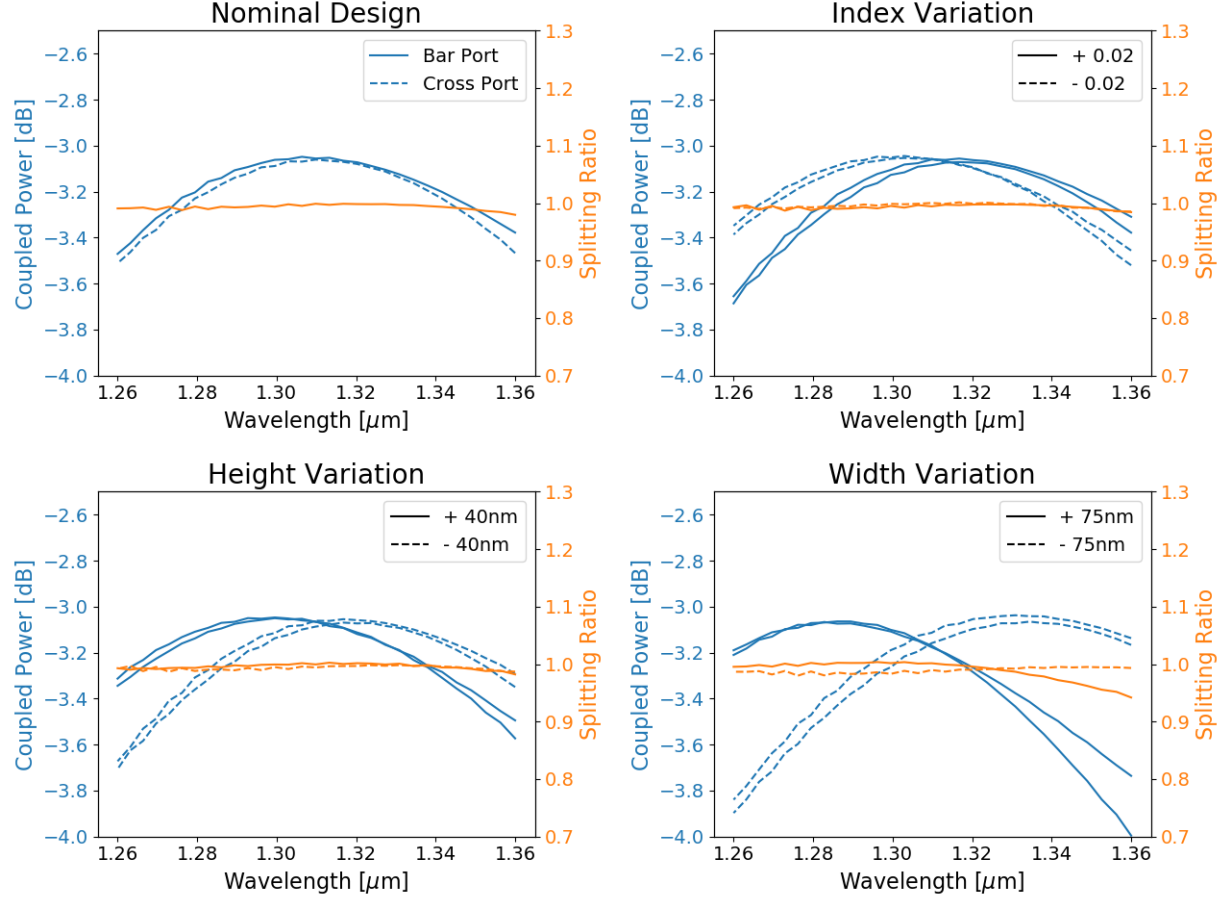


Figure 3.5: Plots of the optimized MMI design transmissions (blue) and splitting ratio (orange), for the nominal design (top left), and under different potential fabrication variances, index (± 0.02 , top right), waveguide height ($\pm 40\text{nm}$, bottom left), waveguide width ($\pm 75\text{nm}$, bottom right)

The device performance as well as the tolerances of the MMI 2×2 coupler are shown in Figure 3.5.

The MMI coupler provides an excellent balance between the output ports, with the splitting ratio between the two arms rarely deviating from unity even factoring in fabrication variance. In the nominal case, an imbalance of $< 0.1\text{dB}$ throughout the wavelength span is achieved. Even with fabrication tolerances factored in, the worst-case imbalance is $< 0.3\text{dB}$. However, in all cases, insertion losses become an issue as wavelength deviates from the optimum, with insertion losses of $< 1\text{dB}$ for nominal and $< 2\text{dB}$ for the worst case. The coupler seems to show additional sensitivity to potential linewidth variations. This is explained by substituting the variations into the variational relationship between the different dimensions of the MMI coupler, which yields

$$2 \frac{|\partial W|}{W} = \frac{|\partial L|}{L} = \frac{|\partial n_{eff}|}{n_{eff}}. \quad (3.9)[45]$$

The MMI coupler shows good promise for interfering LO and the reflection from the DUT for balanced photodetection, but the insertion losses makes it undesirable for isolating the back reflection from the DUT.

3.2.2 Directional Coupler

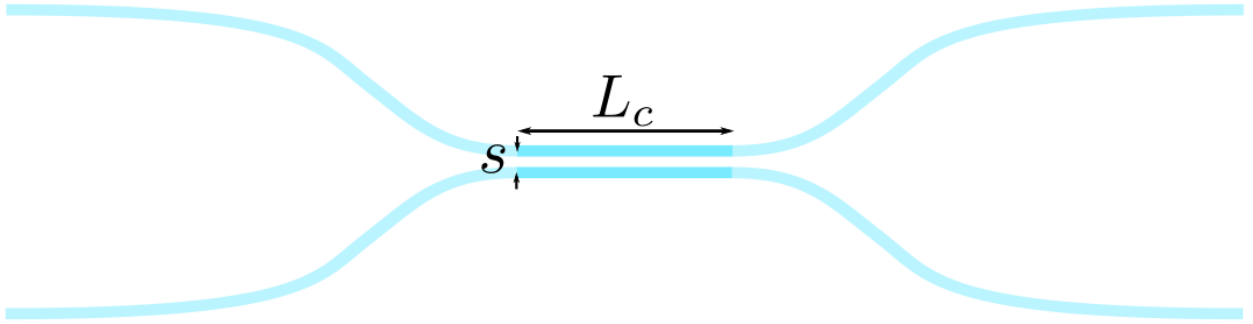


Figure 3.6: The geometric definition of a directional coupler. L_c is the length of the coupling region, s is the centerline separation between the two waveguides in the coupling region.

A directional coupler operates by bringing two parallel waveguides close together, into the coupling region, where the waveguides are separated by a distance s . In the coupling region, the propagating modes in each waveguide become mutually coupled and power transfer between the waveguides occur. The waveguides are then brought apart after reaching the desired power coupling. Following from orthogonal coupled mode theory, the transmission matrix of a directional coupler is

$$T = \begin{bmatrix} \cos\theta - j\cos\phi\sin\theta & -j\sin\phi\sin\theta \\ -j\sin\phi\sin\theta & \cos\theta + j\cos\phi\sin\theta \end{bmatrix}, \quad (3.10)[46]$$

$$\theta = \sqrt{\kappa^2 + \delta^2} L_c, \quad \tan\phi = \kappa/\delta,$$

$$\delta = \Delta\beta/2,$$

where κ is the per-length coupling coefficient, L_c is the length of the coupling region, $\Delta\beta$ is the difference between the propagation constants of the two waveguides, and δ is the detuning factor.

The power in waveguide 2 when light is launched in waveguide 1 is

$$P_2(L) = P_1(0) \frac{\kappa^2}{\kappa^2 + \delta^2} \sin^2 \left(\sqrt{\kappa^2 + \delta^2} L \right), \quad (3.11)$$

where P_1, P_2 are the powers in waveguide 1 and 2 respectively, L is the coupling length. The coupling coefficient κ and detuning factor θ can be related to the difference of the symmetric and antisymmetric supermodes effective index in the coupling region through

$$\sqrt{\kappa^2 + \delta^2} = \frac{\pi}{\lambda} (n_s - n_a), \quad (3.12)[47]$$

where n_s and n_a are the effective index of the symmetric and asymmetric supermodes, respectively.

3.2.2.1 Symmetric directional coupler

In a symmetric directional coupler, the phase detuning factor, δ , is zero and Eq. (3.11) simplifies to

$$P_2(L) = P_1(0) \sin^2(\kappa L), \quad (3.13)$$

where 1:1 balanced output is achieved when

$$L = L_{\pi/4} = \frac{\pi}{4\kappa|_{\lambda_0}}. \quad (3.14)$$

$L_{\pi/4}$ is evaluated at the nominal wavelength λ_0 . Taking the derivative of (3.13) with respect to the wavelength,

$$\frac{d}{d\lambda} P_2(L_{\pi/4}) = \frac{d\kappa}{d\lambda} P_1(0) L_{\pi/4} \sin(2\kappa L_{\pi/4}) \propto \frac{1}{\kappa} \frac{d\kappa}{d\lambda}. \quad (3.15)$$

Using (3.12) to find (3.15) and plotting $\frac{dk}{d\lambda} \frac{1}{\kappa}$ against the separation of the waveguides demonstrate that smaller separation s reduces the wavelength dependence of the device as shown in Figure 3.7.

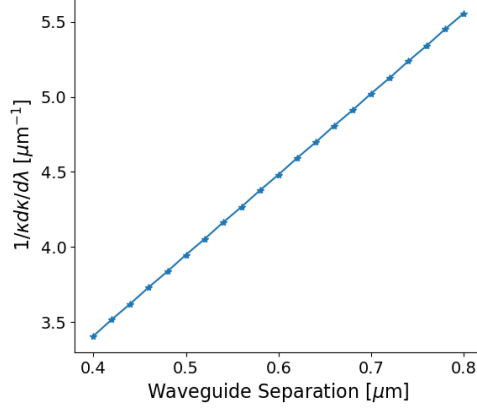


Figure 3.7: Plot of $\frac{1}{k} \frac{dk}{d\lambda}$ against waveguide separation for a symmetric directional coupler at 1310nm

Using a waveguide separation of 400 nm, as limited by the design rules, with $L = 14.07\mu\text{m}$, the symmetric coupler performance and fabrication tolerances are shown in Figure 3.8.

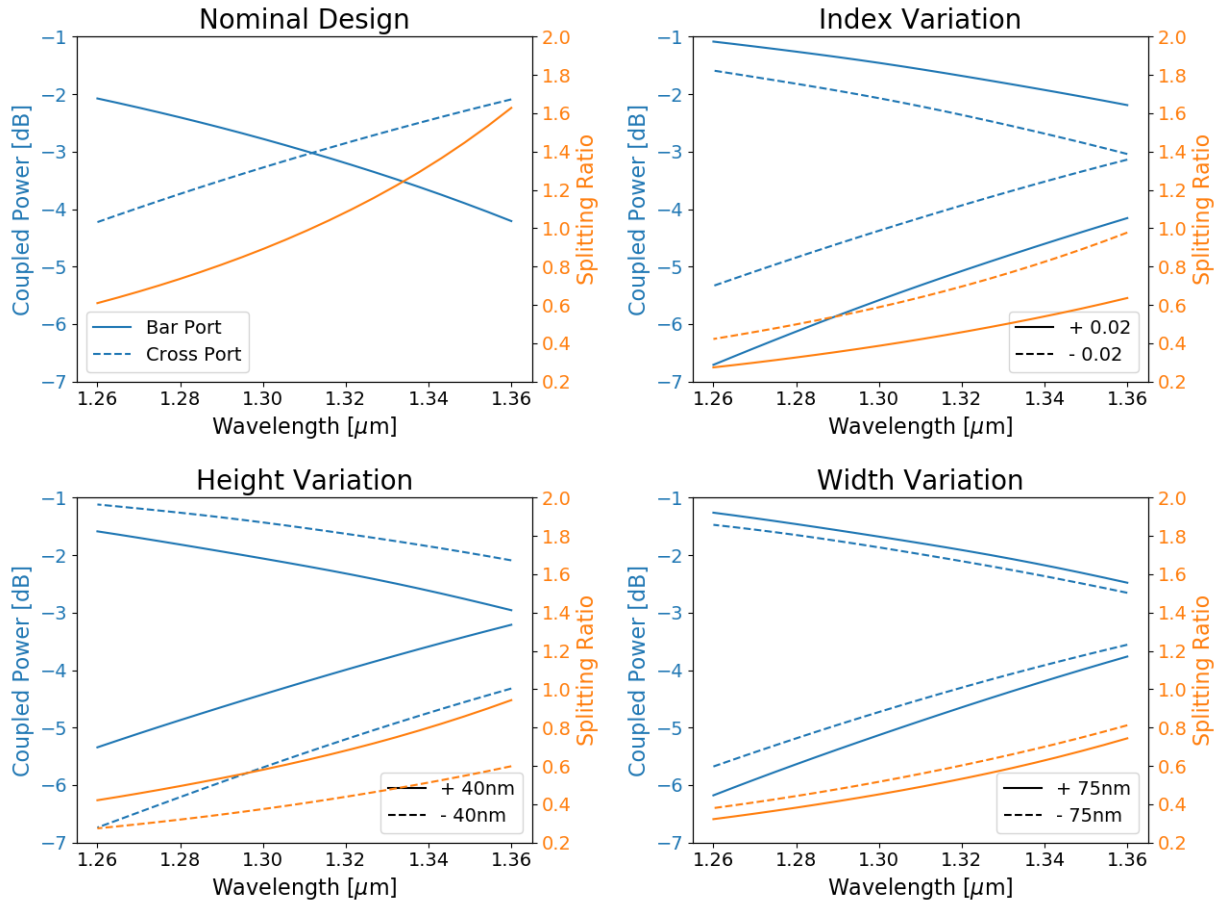


Figure 3.8: Plots of the optimized symmetric directional coupler design transmissions (blue) and splitting ratio (orange), for the nominal design (top left), and under different potential fabrication variances, index (± 0.02 , top right), waveguide height ($\pm 40\text{nm}$, bottom left), waveguide width ($\pm 75\text{nm}$, bottom right)

Conventional directional couplers have negligible insertion loss but suffer from narrowband performance in the balance of the outputs due to waveguide dispersion, resulting in an imbalance of $>2\text{dB}$ in the nominal case. They also exhibit poor fabrication tolerances, which further broadens the imbalance of outputs, making it a risky device in terms of yield. However, with careful phase detuning through breaking the symmetry of the coupling region, the directional coupler output balance and fabrication tolerances can be improved.

3.2.2.2 Asymmetric Directional Coupler

By introducing asymmetry between the two waveguides of a directional coupler, the phase detuning factor δ to become nonzero. This additional asymmetry parameter enables the reduction of maximum coupled power from one waveguide to another to a desired ratio. This introduces a new degree of freedom which opens the possibility of designing a directional coupler that, instead of a monotonic relationship between coupling ratio with wavelength, can instead have a first-order dependence on wavelength removed at the desired coupling ratio. [46], [48]. This asymmetry can be introduced by choosing different waveguide widths for the two parallel waveguides, but this type of asymmetry is generally very sensitive to fabrication variations in the waveguide width [49], [50]. Alternatively, the asymmetry may be introduced by curving the coupling region of a symmetric directional coupler and has been explored as a fabrication tolerant approach to breaking the symmetry of directional couplers.[40], [48], [50], [51]

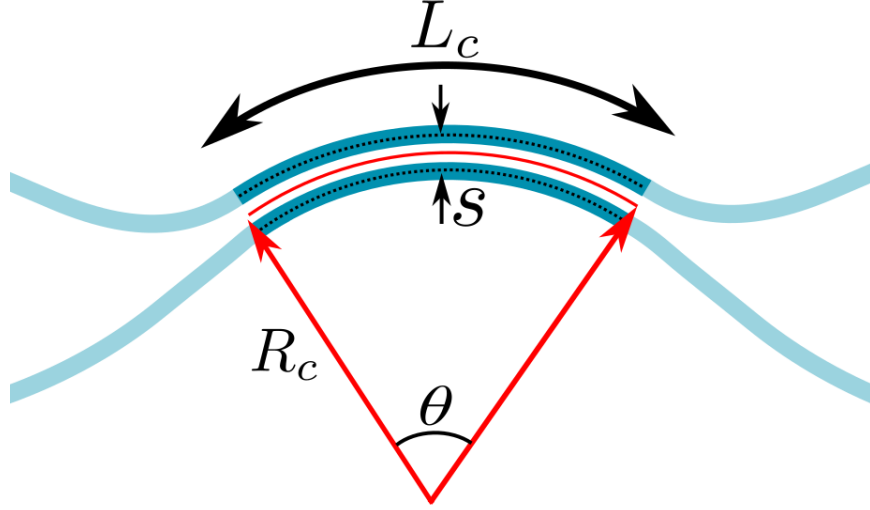


Figure 3.9: The geometric definition of a curved coupling region. R_c is the centerline bend radius of the coupling region, L_c is the length of the coupling region traversing an angle of θ , s is the centerline separation between the waveguides in the coupling region.

The difference in phase accumulated between two waveguides in a curved geometry about a central radius (R_c) with centerline separation (s) over coupling distance L traversing θ radians is

$$\beta \left(R_c + \frac{s}{2} \right) \theta - \beta \left(R_c - \frac{s}{2} \right) \theta = s\beta\theta = \Delta\beta R_c\theta, \quad (3.16)$$

which leads to a difference in propagation constant mismatch ($\Delta\beta$) along the centerline of the coupling region of

$$\Delta\beta = s\beta/R_c. \quad (3.17)$$

By extracting the coupling coefficient through the effective indices of the symmetric and antisymmetric mode for a straight coupling region, we can estimate the central radius and coupling length of the curved coupler for a desired maximum coupling ratio C provided the bend is weak, as follows,

$$C = \frac{\kappa^2}{\left(\frac{\Delta\beta}{2}\right)^2 + \kappa^2} = \frac{\left(\frac{\pi}{\lambda}(n_s - n_a)\right)^2}{\left(\frac{s\beta}{R_c}\right)^2 + \left(\frac{\pi}{\lambda}(n_s - n_a)\right)^2}. \quad (3.18)$$

Manipulating (3.18) to isolate R_c gives the following relation

$$R_c = \frac{2n_{\text{eff}s}}{(n_s - n_a)} \sqrt{\frac{C}{1-C}}, \quad (3.19) \quad [48]$$

and the length of the coupling region for the curved coupler (L_{curved}) is

$$L_{\text{curved}} = \sqrt{C} L_{\text{straight}}, \quad (3.20)$$

where L_{straight} is the coupling length for 100% power transfer from waveguide 1 to 2 in a straight directional coupler with the same waveguide separation.

The power coupled from the waveguide 1 to 2 when launched in waveguide 1 is

$$P_2(L) = C P_1(0) \sin^2(\kappa' L). \quad (3.21)$$

Following (3.19) and (3.20), we get the initial estimates for the central radius and coupling length by setting $C = 0.5$ to find $R_c = 79.3\mu\text{m}$ and $L_c = 20.1\mu\text{m}$. The calculated coupling ratio according to (3.21) is shown in Figure 3.10

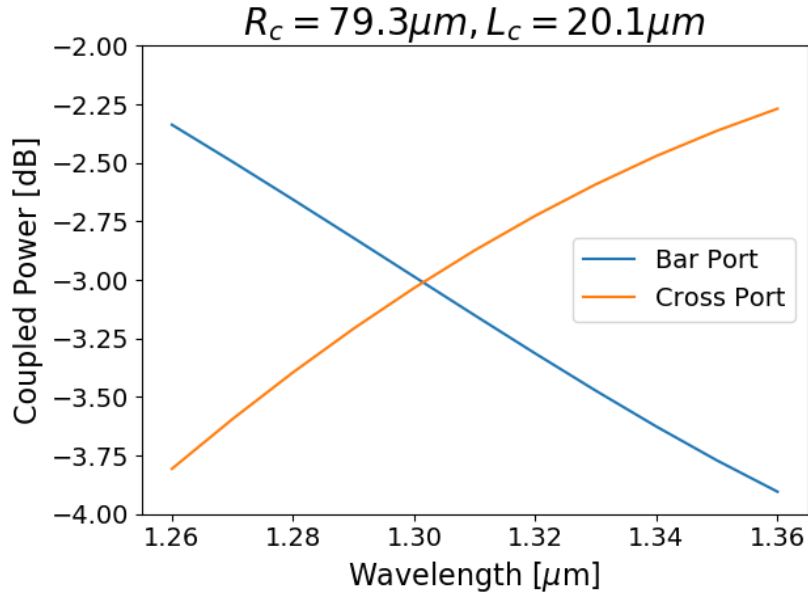


Figure 3.10: Calculated bar and cross port transmissions for the curved coupler with $R_c = 79.3\mu\text{m}$, $L_c = 20.1\mu\text{m}$

The curvature flattens the wavelength response compared to the symmetric coupler; nevertheless, the coupler exhibits significant wavelength dependence in the coupling ratio. To further refine the estimate of the curvature, we can compute the coupling constant κ and detuning constant δ from (3.12) and (3.17) for wavelengths around 1310nm and balance the derivative of (3.21),

$$\frac{dP_2(L)}{d\lambda} = P_1(0) \left(\frac{dC}{d\lambda} \sin^2(\kappa' L) + C \frac{d\kappa'}{d\lambda} L \sin(2\kappa' L) \right). \quad (3.22)$$

The R_c and L are swept and the calculated $dP_2/d\lambda$ and P_2 is shown in Figure 3.11.

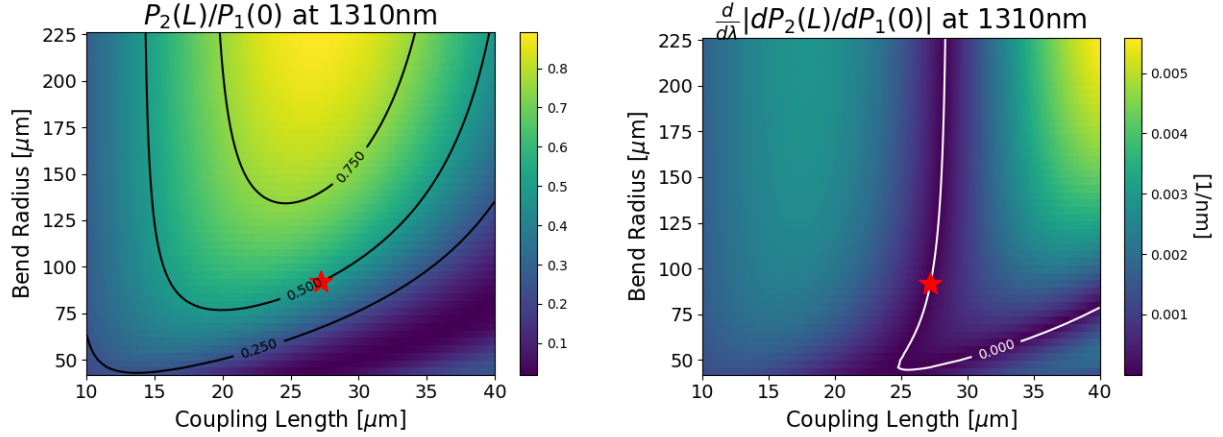


Figure 3.11: Plot of coupling ratio (left) and its derivative with respect to wavelength (right) at 1310nm. Star indicates the optimized parameters.

To find the optimal parameters, the intersection of the contour lines $dP_2/d\lambda = 0$ and $P_2(L)/P_1(0) = 0.5$ is taken which results in the parameter estimates of $R_c = 91.8\mu m, L = 27.2\mu m$.

Checking the bend radius in MODE solutions shows negligible radiation losses at $R_c = 91.8\mu m$ which means the curved coupler should suffer minimal insertion losses. The calculated coupler performance according to (3.21) is shown in Figure 3.12.

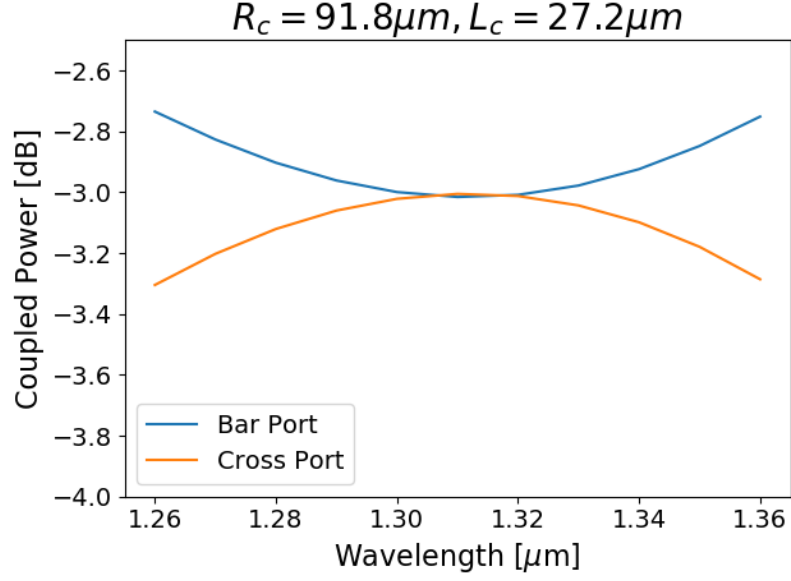


Figure 3.12: Calculated bar and cross port transmissions of curved coupler with $R_c = 91.8\mu\text{m}$, $L_c = 27.2\mu\text{m}$

This curved waveguides generate a much flatter wavelength response than the initial curvature in Figure 3.10, however since the coupler is scored based on the worst performance in the wavelength range, the optimal transmission would have the bar and cross port transmission overlap more, as shown in Figure 3.13. Iterative optimization of R_c and L through FDTD simulation yields the final optimal parameters which includes the influence of coupling between the waveguides bending in before and out after the coupling region, the optimized parameters are found in Table 3.2.

Table 3.2: Table of curved Directional coupler parameters, for initial guess and optimized design

Parameters	Initial Guess	Optimized Parameters
R_c [μm]	91.8	89.5
L_c [μm]	27.2	20.0

The final performance and the sensitivities of various fabrication errors of the curved coupler are shown in Figure 3.13

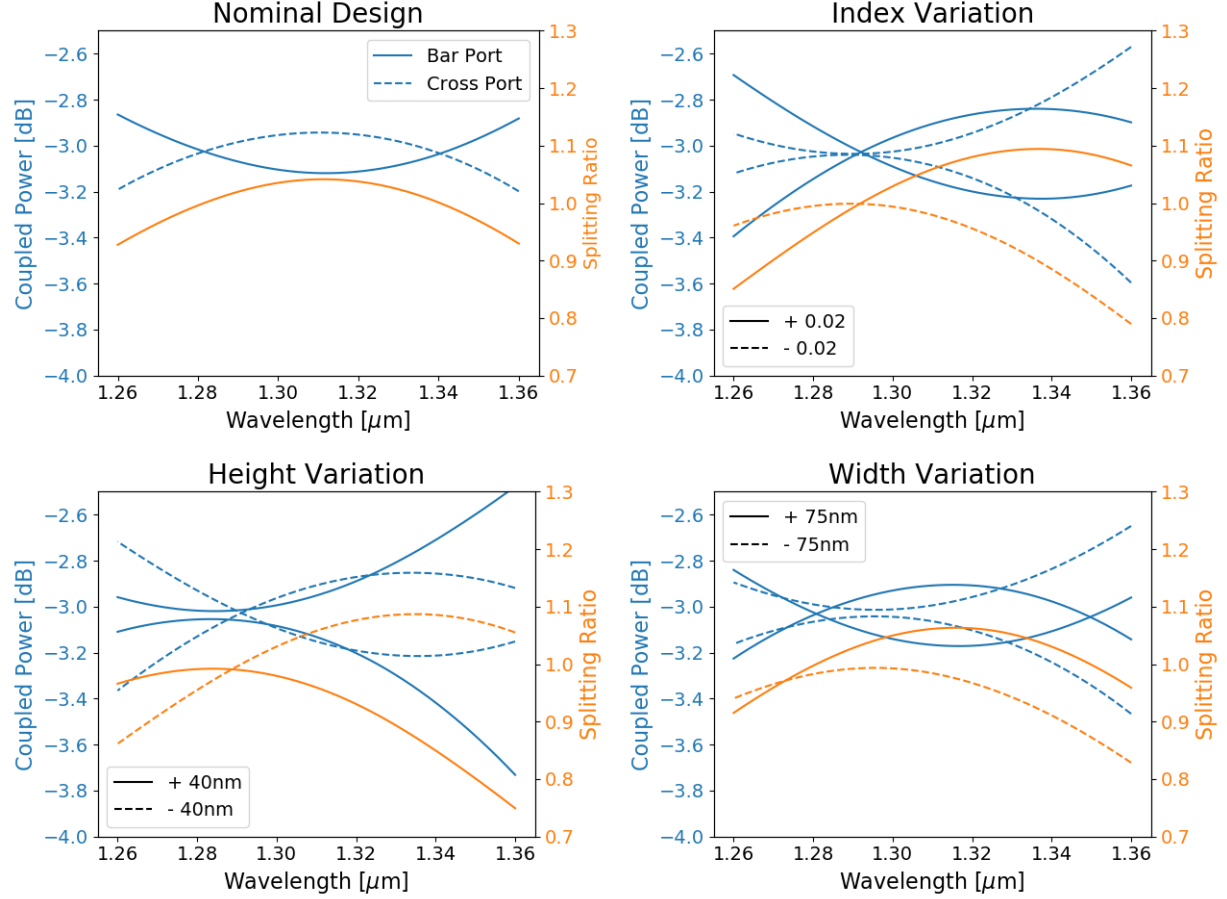


Figure 3.13: Plots of the optimized curved coupler design transmissions (blue) and splitting ratio (orange), for the nominal design (top left), and under different potential fabrication variances, index (± 0.02 , top right), waveguide height ($\pm 40\text{nm}$, bottom left), waveguide width ($\pm 75\text{nm}$, bottom right)

The curved asymmetric directional coupler, like the symmetric directional coupler shows negligible insertion losses. However, by eliminating a first-order wavelength dependence on the coupling ratio at the center wavelength, the balance of the outputs of the curved directional coupler is vastly improved compared to the symmetric version, resulting in a coupling imbalance of less than 0.4dB in the nominal case. Furthermore, the curved coupler shows resilience to linewidth variations that the asymmetric width directional coupler is vulnerable to, and performance is not significant impacted by index and height variations, in all considered cases the imbalance remains $< 1\text{dB}$.

3.2.3 Adiabatic coupler

Adiabatic 2×2 couplers relies on the principle of adiabatic evolution of modes through gradual changes in the waveguide cross-section over long propagation lengths (\sim mm) [52][53]. This type of 2×2 coupler is generally very broadband but are long. The very large device footprint conflicts with the chip real estate required for the number of 2×2 couplers needed in an OFDR system. Therefore, the adiabatic couplers were not considered for this thesis. Compact footprint adiabatic couplers have been demonstrated, but require subwavelength features for dispersion engineering, which is unfeasible on a foundry process due to low tolerance for fabrication variations and feature size limitations [54].

3.3 Comparison of 2×2 Coupler Options

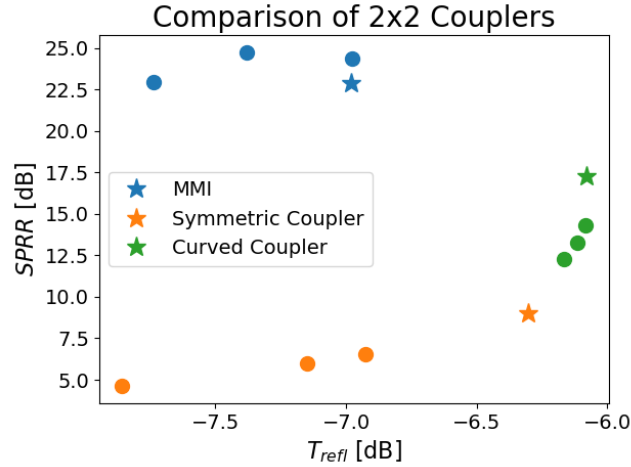


Figure 3.14: A comparison of designed 2×2 couplers on the basis of single port rejection ratio (SPRR) and losses accrued from isolating the back reflection from the DUT (T_{refl}). Stars are the nominal designs, and dots are performances after applying fabrication variations in the index, waveguide height, and waveguide width.

Amongst the explored options for 2×2 couplers, MMIs provide the best output balance overall and are the most tolerant to fabrication variations. They achieve a SPRR >20 dB, but their high insertion losses lead to additional losses of >1 dB from the optimal -6 dB when used to isolate reflections. Curved couplers excel in isolating the back reflection from the DUT due to the combination of output balance and negligible insertion losses, with losses <0.25 dB from the optimal,

though its performance is inferior to MMI coupler in terms of the SPRR ($<20\text{dB}$), which can be further degraded with fabrication variations. The symmetric directional coupler, even in the optimal case has worse performance than the curved counterpart largely due to narrowband performance in terms of losses from reflection isolation ($>0.25\text{dB}$) and SPRR ($<10\text{dB}$). The performance is worsened when there are fabrication variances. Thus, the MMI coupler and the curved coupler are chosen for further exploration in the integrated optic implementation of OFDR.

3.4 Conclusion

We have explored and evaluated several options for 2×2 coupler for the role of isolating the back reflection from the DUT and facilitating the interference between the LO and the back reflection from the DUT, such as MMIs, symmetric and asymmetric directional. Adiabatic couplers were not explored due to the amount of chip real estate required which makes on chip OFDR implementation impractical.

The evaluation of the different options for 2×2 couplers shows that MMIs has excellent output balance which leads to good performance for mixing the LO and reflection from DUT in a balanced detection setup, as indicated by the high SPRR. However, the growing insertion losses as wavelength deviates from the center leads additional losses when used to isolate reflections from the DUT. The curved coupler performs well in isolating reflections from the DUT due to minimal insertion losses, but it has inferior SPRR compared to MMIs. Symmetric directional couplers do not perform as well as MMIs or curved directional couplers.

Thus, the MMI and curved couplers are the most promising candidates for fabrication and testing, potentially for a hybrid configuration in which the curved coupler isolates the back reflection from the DUT and the MMI facilitates the mixture between the LO and reflections from the DUT.

Chapter 4

Test Structures and Measurement Setup

In this chapter, we detail the test structures designed and fabricated for the purpose of characterizing the SiN-on-Si photonics platform and devices needed for the integrated optic implementation of OFDR. The devices include the general components in Chapter 2 as well as the 2×2 couplers designed in Chapter 3. This chapter will conclude with the measurement setup and methodologies for measuring the test structures.

4.1 Test Structures

Several test structures were designed to characterize some of the passive devices described in Chapter 2, as well as the 2×2 coupler candidates designed in Chapter 3, all of which will be the building blocks of an integrated photonic OFDR implementation.

4.1.1 Polarization Calibration Structures



Figure 4.1: *The layout of a polarization calibration structure*

Polarization calibration structures are edge coupled and consists of numerous tight bends with radii of 10μm on the Si photonic layer are placed on multiple locations on the fabricated chips to calibrate and verify the polarization being coupled onto the chip prior to each measurement. This calibration

structure enables us to ensure the measurements are characterized with the TE polarization. The tight bends have high polarization dependent losses favoring the TE mode which will allow the adjustment of polarization controllers to minimize the losses as to calibrate the input polarization.

4.1.2 Edge coupler Calibration Structures

An edge coupler calibration structure is a straight waveguide routing from one facet of the chip to the other. It is used to extract the edge coupler losses by factoring out external losses from the testing setup.

4.1.3 Waveguide Cutback Structures

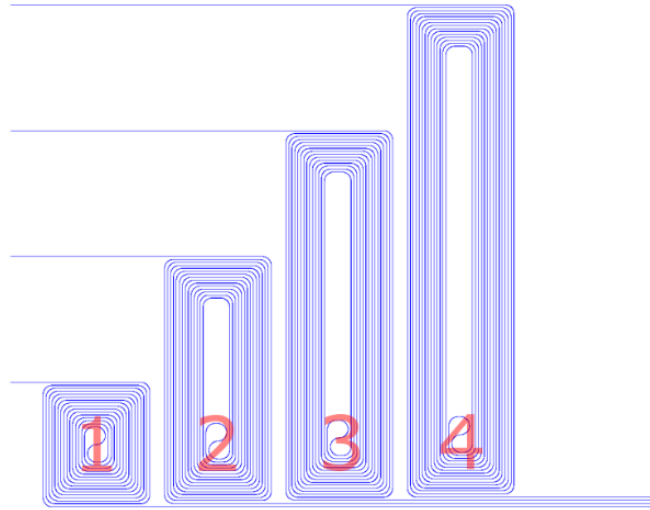


Figure 4.2: The layout of waveguide cutback spiral structures labelled (1, 2, 3, 4) have relative pathlength differences of (0, 1.2, 2.4, 3.6)cm.

Waveguide spiral structures are edge coupled test structures placed with path length differences of (0, 1.2, 2.4, 3.6)cm of straight waveguide sections between the spirals (1, 2, 3, 4), while keeping the rest of the structure functionally identical. By measuring the losses accrued in each of the waveguide spiral structure and performing a linear fit of the transmission against the waveguide length, the per-length waveguide propagation losses can be determined from the slope of the fit.

4.1.4 Transition Cutback Structures

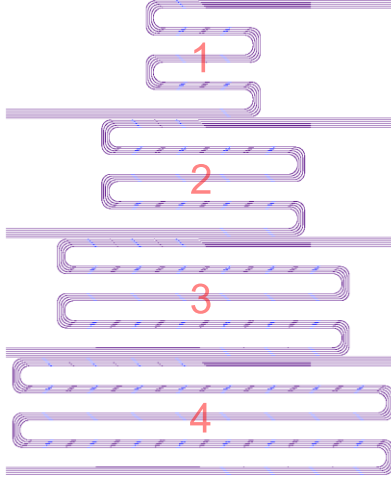


Figure 4.3: The layout of interlayer transition cutback structure labeled (1, 2, 3, 4) have (12, 38, 58, 78) interlayer transitions

Interlayer transitions are characterized by edge coupled test structures placed with many interlayer transitions in series with randomized intervals to prevent buildup of resonant reflections. [12] Each structure (1, 2, 3, 4) has incrementally many interlayer transitions (18, 38, 58, 78). The insertion loss for the interlayer transitions can be obtained by performing a linear fit on the measured losses as a function of the number of transitions.

4.1.5 MMI Cutback Structure

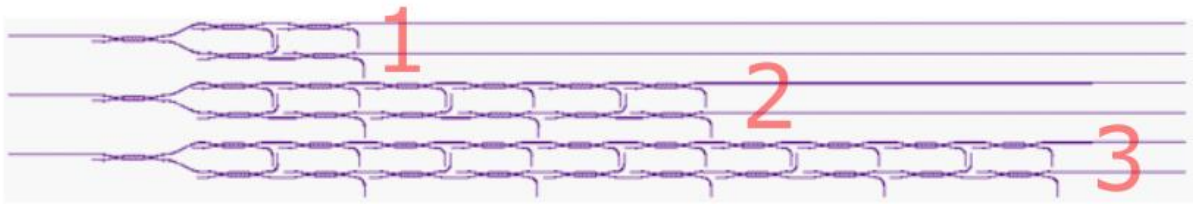


Figure 4.4: The layout of MMI cutback structures in bar and cross port configurations labeled (1, 2, 3) have (3, 7, 10) consecutive MMIs

To determine the loss of the MMI, cutback structures for (3, 7, 10) consecutive bar and cross ports of the MMI couplers are connected in series in test structures (1, 2, 3) and placed to directly characterize their bar and cross port transmission through linear fitting of the measured losses. The

unbalanced Mach-Zehnder Interferometer method in the next section does not work well for MMIs due to the MMI loss.

4.1.6 Unbalanced Mach-Zehnder Interferometer

Edge-coupled unbalanced Mach-Zehnder interferometers (UMZI) test structures are used to characterize the coupling ratio of the curved directional couplers indirectly through the extinction ratio of the peaks and troughs of the transmission spectrum. [55]

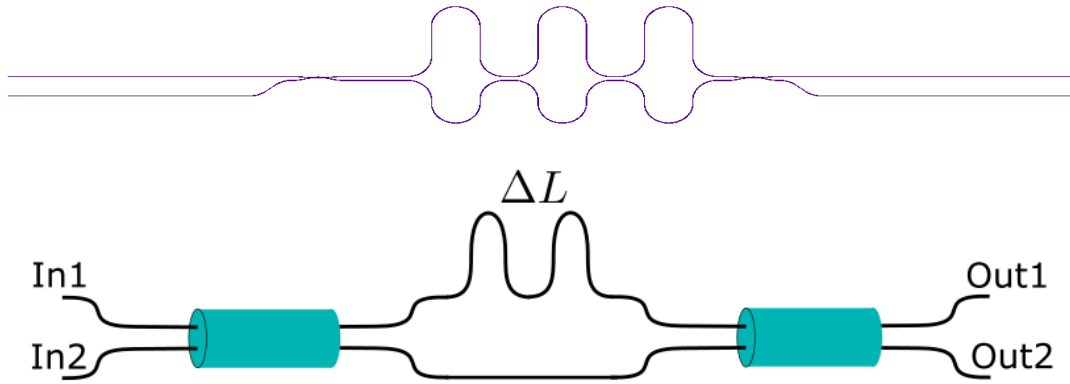


Figure 4.5: The unbalanced Mach Zehnder interferometer (UMZI) test structure. Top: Layout representation, Bottom: Schematic representation, where In1, In2 are the input ports 1 and 2, respectively and Out1, Out2 are the output ports 1 and 2, respectively. ΔL is the excess path length between the longer arm and the shorter arm of the UMZI structure.

We describe how this method works by analyzing the transmission spectrum of the UMZI. The transmission matrix (S_{DC}) for the directional couplers 1 and 2 are

$$S_{DC1} = \begin{bmatrix} t_{b1} & t_{c1} \\ t_{c1} & t_{b1}^* \end{bmatrix}, S_{DC2} = \begin{bmatrix} t_{b2} & t_{c2} \\ t_{c2} & t_{b2}^* \end{bmatrix}. \quad (4.1)$$

where t_b, t_c are the lumped bar and cross field transmission coefficients, respectively. The

transmission matrix (S_{prop}) for the unbalanced paths with a length difference of ΔL between the directional couplers 1 and 2 is

$$S_{prop} = e^{(-\alpha+j\beta)L} \begin{bmatrix} e^{(-\alpha+j\beta)\Delta L} & 0 \\ 0 & 1 \end{bmatrix}. \quad (4.2)$$

where α, β are the attenuation and propagation constant through the SiN strip waveguide, and L is the shared path length between the two arms of the UMZI test structure.

The total S matrix for the UMZI test structure is

$$S = S_{DC1} S_{prop} S_{DC2} = e^{(-\alpha+j\beta)L} \begin{bmatrix} t_{b1}t_{b2}e^{(-\alpha+j\beta)\Delta L} + t_{c1}t_{c2} & t_{b1}t_{c2}e^{(-\alpha+j\beta)\Delta L} + t_{c1}t_{b2}^* \\ t_{b2}t_{c1}e^{(-\alpha+j\beta)\Delta L} + t_{b1}^*t_{c2} & t_{c1}t_{c2}e^{(-\alpha+j\beta)\Delta L} + t_{b1}^*t_{b2}^* \end{bmatrix}. \quad (4.3)$$

For an optical input at In1 and In2 in Figure 4.5, we have the output ports Out1 and Out2, the

intensities $I_{in1out1}, I_{in1out2}, I_{in2out1}$, and $I_{in2out2}$ are given as follows:

$$\begin{aligned} I_{in1out1} &= S_{11}S_{11}^* = e^{(-2\alpha)L} (|t_{b1}t_{b2}|^2 e^{-2\alpha\Delta L} + |t_{c1}t_{c2}|^2 + \cos(\beta\Delta L + \phi_b - \phi_c) e^{-\alpha\Delta L} |t_{b1}t_{b2}t_{c1}t_{c2}|^2), \\ I_{in1out2} &= S_{12}S_{12}^* = e^{(-2\alpha)L} (|t_{b1}t_{c2}|^2 e^{-2\alpha\Delta L} + |t_{b2}t_{c1}|^2 + \cos(\beta\Delta L + 2\phi_c) e^{-\alpha\Delta L} |t_{b1}t_{b2}t_{c1}t_{c2}|^2), \\ I_{in2out1} &= S_{21}S_{21}^* = e^{(-2\alpha)L} (|t_{b2}t_{c1}|^2 e^{-2\alpha\Delta L} + |t_{b1}t_{c2}|^2 + \cos(\beta\Delta L + 2\phi_c) e^{-\alpha\Delta L} |t_{b1}t_{b2}t_{c1}t_{c2}|^2), \\ I_{in2out2} &= S_{22}S_{22}^* = e^{(-2\alpha)L} (|t_{c1}t_{c2}|^2 e^{-2\alpha\Delta L} + |t_{b1}t_{b2}|^2 + \cos(\beta\Delta L + 2\phi_c) e^{-\alpha\Delta L} |t_{b1}t_{b2}t_{c1}t_{c2}|^2). \end{aligned} \quad (4.4)$$

As the wavelength of the optical input is swept, the $\beta\Delta L$ term changes rapidly and an interference pattern is formed, with extinction ratios between the peaks and the troughs of

$$\begin{aligned} ER_{11} &= \frac{\max(I_{in1out1})}{\min(I_{in1out1})} = \frac{(e^{-\alpha\Delta L}|t_{b1}t_{b2}| + |t_{c1}t_{c2}|)^2}{(e^{-\alpha\Delta L}|t_{b1}t_{b2}| - |t_{c1}t_{c2}|)^2}, \\ ER_{12} &= \frac{\max(I_{in1out2})}{\min(I_{in1out2})} = \frac{(e^{-\alpha\Delta L}|t_{b1}t_{c2}| + |t_{b2}t_{c1}|)^2}{(e^{-\alpha\Delta L}|t_{b1}t_{c2}| - |t_{b2}t_{c1}|)^2}, \\ ER_{21} &= \frac{\max(I_{in2out1})}{\min(I_{in2out1})} = \frac{(e^{-\alpha\Delta L}|t_{b2}t_{c1}| + |t_{b1}t_{c2}|)^2}{(e^{-\alpha\Delta L}|t_{b2}t_{c1}| - |t_{b1}t_{c2}|)^2}, \\ ER_{22} &= \frac{\max(I_{in2out2})}{\min(I_{in2out2})} = \frac{(e^{-\alpha\Delta L}|t_{c1}t_{c2}| + |t_{b1}t_{b2}|)^2}{(e^{-\alpha\Delta L}|t_{c1}t_{c2}| - |t_{b1}t_{b2}|)^2}. \end{aligned} \quad (4.5)$$

Manipulating the expressions from Eq. (4.5), the extinction ratios (ER) can be combined to form

composite parameters M_{11}, M_{12}, M_{21} , and M_{22} .

$$M_{11} = \frac{\sqrt{ER_{11}} + 1}{\sqrt{ER_{11}} - 1} = \left(\frac{e^{-\alpha\Delta L} |t_{b1} t_{b2}|}{|t_{c1} t_{c2}|} \right)^j \quad M_{12} = \frac{\sqrt{ER_{12}} + 1}{\sqrt{ER_{12}} - 1} = \left(\frac{e^{-\alpha\Delta L} |t_{b1} t_{c2}|}{|t_{b2} t_{c1}|} \right)^k \quad (4.6)$$

$$M_{21} = \frac{\sqrt{ER_{21}} + 1}{\sqrt{ER_{21}} - 1} = \left(\frac{e^{-\alpha\Delta L} |t_{b2} t_{c1}|}{|t_{b1} t_{c2}|} \right)^l \quad M_{22} = \frac{\sqrt{ER_{22}} + 1}{\sqrt{ER_{22}} - 1} = \left(\frac{e^{-\alpha\Delta L} |t_{c1} t_{c2}|}{|t_{b1} t_{b2}|} \right)^m$$

$$j, k, l, m = \pm 1$$

Combining the parameters found in (4.6), we get

$$M_{11} M_{22} = \frac{e^{-\alpha\Delta L(j+m)} |t_{b1} t_{b2}|^{j-m}}{|t_{c1} t_{c2}|^{j-m}} = \begin{cases} e^{-2\alpha\Delta L}, & \text{if } j = 1, m = 1 \\ e^{2\alpha\Delta L}, & \text{if } j = -1, m = -1 \end{cases} \quad (4.7)$$

$$\frac{M_{11}}{M_{22}} = \frac{e^{-\alpha\Delta L(j-m)} |t_{b1} t_{b2}|^{j+m}}{|t_{c1} t_{c2}|^{j+m}} = \begin{cases} e^{-2\alpha\Delta L}, & \text{if } j = 1, m = -1 \\ e^{2\alpha\Delta L}, & \text{if } j = -1, m = 1 \end{cases}$$

By comparing the expressions in (4.7) with the estimated waveguide losses from measurements, we

can determine the signs of j and m . j is positive if $e^{-\alpha\Delta L} |t_{b1} t_{b2}| > |t_{c1} t_{c2}|$, and is negative

otherwise. m is positive if $e^{-\alpha\Delta L} |t_{c1} t_{c2}| > |t_{b1} t_{b2}|$ and is negative otherwise. A similar approach can

be done for k and l . Once j, k, l, m are known, the parameters $M_{11}, M_{12}, M_{21}, M_{22}$ can be combined to

obtain

$$M_{11}^a M_{12}^b M_{21}^c M_{22}^d = e^{-\alpha\Delta L(j'+k'+l'+m')} \left| \frac{t_{b1}}{t_{c1}} \right|^{(j'+k'-l'-m')} \left| \frac{t_{b2}}{t_{c2}} \right|^{(j'+l'-k'-m')}, \quad (4.8)$$

$$j', k', l', m' = aj, bk, cl, dm$$

where $a, b, c, d = \pm 1$ and are freely chosen

where the value of j', k', l', m' , can be freely set to +1 or -1 by choosing the correct corresponding

value for a, b, c, d . By choosing certain values for j', l', m' , (4.8) becomes

$$\{j' = 1, k' = 1, l' = -1, m' = -1\} \Rightarrow \left| \frac{t_{b1}}{t_{c1}} \right|^4, \quad (4.9)$$

$$\{j' = 1, k' = -1, l' = 1, m' = -1\} \Rightarrow \left| \frac{t_{b2}}{t_{c2}} \right|^4.$$

By assuming that the directional couplers are lossless,

$$|t_b|^2 = (1 - |t_c|^2), \quad (4.10)$$

which is a reasonable assumption due to the weak curvature of the coupling region combined with the low SiN propagation losses [32], the field transmission coefficients can be characterized from their ratio obtained in (4.9).

The interference fringes generated by the UMZI structure have a free spectral range $\Delta\lambda_{FSR}$ of

$$\Delta\lambda_{FSR} = \frac{\lambda_0^2}{n_g \Delta L}. \quad (4.11)$$

Where λ_0 is the center wavelength, n_g is the group index of the waveguide. The simulated group index of the waveguide dimensions chosen in Chapter 2 is shown in Figure 4.6.

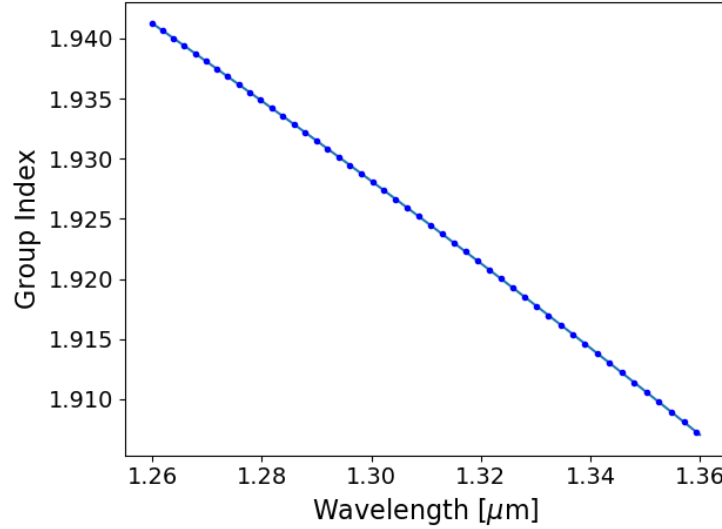


Figure 4.6: Simulated group index of SiN strip waveguide as defined in Chapter 2. Dots are calculated interferogram cycles with $\Delta L = 420\mu m$

ΔL is chosen to be 420um, which corresponds with a $\Delta\lambda_{FSR}$ of $\sim 2nm$, provides ~ 48 data points in the targeted wavelength range of $1.26\mu m$ to $1.36\mu m$, as illustrated in Figure 4.6.

4.1.7 Germanium photodetector

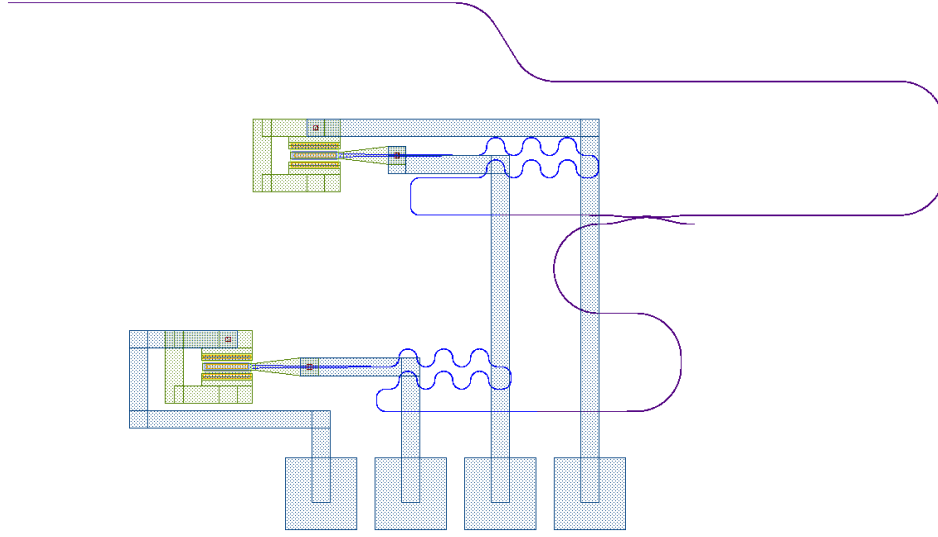


Figure 4.7: The layout of a 2×2 PD test structure

To cross-validate the measurements from the UMZI and cutback structures for the directional couplers and the MMI couplers respectively, germanium PDs are connected to the two output ports of the curved coupler and MMI couplers through a polarization filter in order to directly characterize the coupling and insertion loss of the 2×2 couplers.

4.2 Measurement setup

The optical measurements were made with the TLS (Agilent 81600b), passing through a polarization controller (Oz Optics FPC-100) and edge coupled onto the chip through a lensed fiber. For each measurement, the polarization calibration structure was used to calibrate the light input to be TE polarized. The edge coupled output on the other side of the chip is captured by another lensed fiber connected to a polarization analyzer (Oz-Optics FPR-01-3A3A-1550-S-S-1) and then measured with an optical power meter (Agilent N7744A). The wavelength of the TLS is swept from 1260nm to 1360nm to capture the spectral characteristic of the test structures.

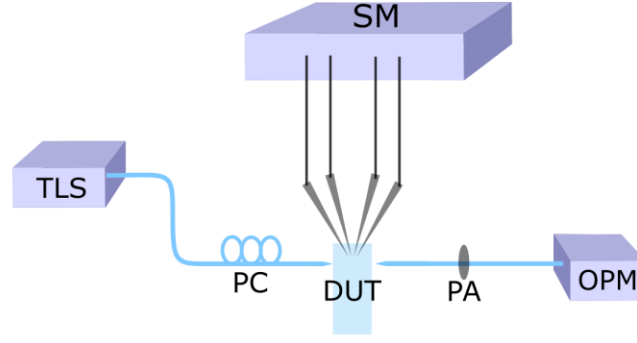


Figure 4.8: Schematic representation of the measurement setup. DUT: device under test TLS: Tunable laser source; PC: polarization controller; SM: source meter; PA: Polarization analyzer; OPM: optical power meter

For the electrical PD measurements, after initial input polarization calibration, four needle probes were brought to contact the metal pads connected to the two PDs attached to the output ports of the coupler in Figure 4.7, which are connected to an electrical source meter (Keithley 2602B).

Dependence of the forward bias current on the needle probe placement was observed, likely due to varying contact resistance due to probe placement. To match the contact resistance, initial voltage sweeps are performed and the IV curves between the two PDs are matched by adjusting the needle probe placement. Light is launched into the coupler under test and the PD currents were measured under a reverse bias of -1V as the wavelength of the TLS is stepped from 1260nm to 1360nm.

4.3 Conclusion

In this chapter, we described the test structures that were placed to characterize the input polarization, edge couplers, waveguide losses, interlayer transition losses and the 2×2 coupler candidates. Cutback structures are used to characterize the losses of waveguide propagation, interlayer transitions, MMI couplers. The theory behind using UMZI test structures to characterize the coupling of the curved directional coupler is given. The measurement setup and methodology for the optical and electrical measurements are described.

Chapter 5

Measurement Results

In this chapter, the measurement results of the test structures detailed in Chapter 4 are shown. The measured results for waveguide propagation losses and general devices will be compared with previously reported results from similar platforms. The bar and cross port transmissions of the 2×2 coupler candidates are extracted from measurements. Their performance as it pertains to their roles of isolating the reflections from DUT and facilitating the mixture of LO and reflections from the DUT are evaluated based on the extracted transmissions.

5.1 Waveguide Propagation

The propagation losses for the strip waveguides with specifications detailed in Chapter 2 were measured with TE polarization on the spiral cutback structures detailed in Chapter 4. The results for the SiN and Si strip waveguides are shown in Figure 5.1

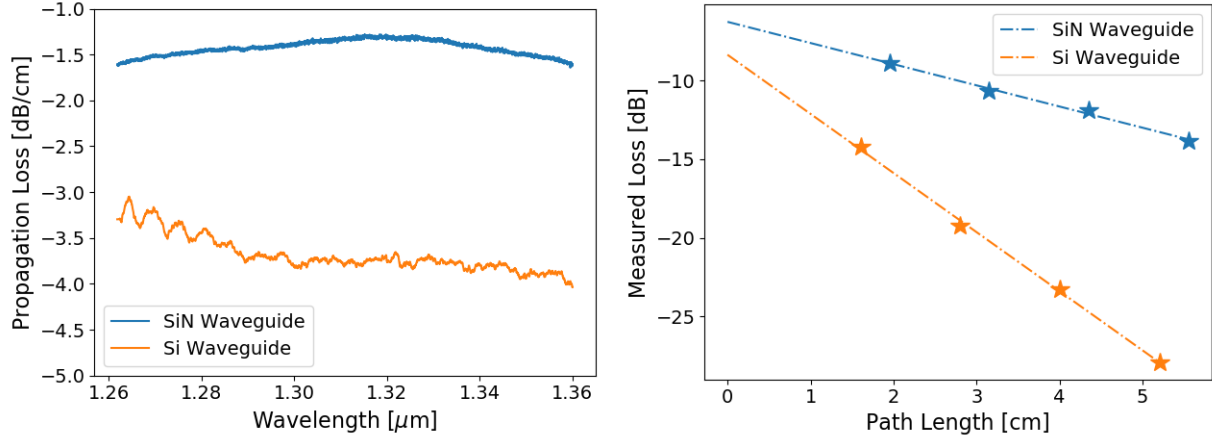


Figure 5.1 (left) Plot of interpolated waveguide propagation losses for SiN and Si strip waveguides. (right) Raw cutback measurements for SiN and Si strip waveguide spirals at 1310nm

The interpolated propagation losses differs with previously reported results for similar waveguides. [12] notably the SiN propagation loss is obtained as $\sim 1.5\text{dB/cm}$ compared to $\sim 0.3\text{dB/cm}$ reported previously. This is likely due to variations in the deposition conditions of the PECVD SiN leading to a different composition. Si strip waveguide propagation loss is obtained as $\sim 3.5\text{dB/cm}$ compared to $\sim 5\text{dB/cm}$ reported previously. This discrepancy may be the result of reduced scattering due to smoother sidewalls.

5.2 Interlayer Transitions

The interlayer transition insertion loss was measured with TE polarization on the cutback structures detailed in Chapter 4. The results for the interlayer transitions are shown in Figure 5.2.

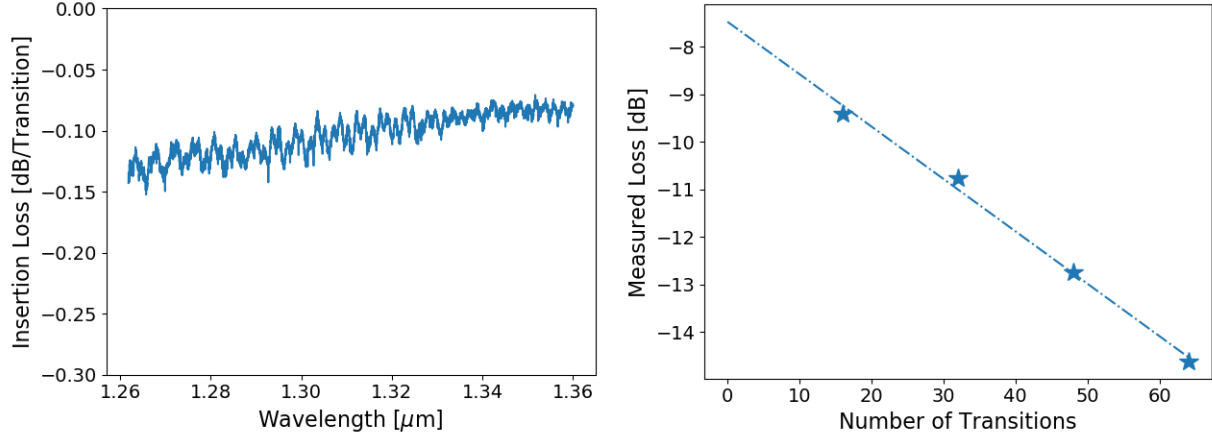


Figure 5.2: (left) Plot of interpolated interlayer transition insertion loss. (right) Raw cutback measurements of interlayer transition test structures at 1310nm.

The interlayer transition losses from the cutback structures are ~ 0.1 dB/transition, compared to the 0.15 dB/transition reported previously. [12] This falls within the expectation as the smaller tip width ($w_{SiN\ tip} = 200\text{nm}, w_{Si\ tip} = 180\text{nm}$) compared to the reference ($w_{SiN\ tip} = 300\text{nm}, w_{Si\ tip} = 200\text{nm}$) [12] may account for the reduced insertion loss due to lower scattering loss at the blunt tip interface.

5.3 Photodetector Responsivity

Photodetector responsivity was measured through a directional coupler where the current from the two photodetectors connected to the two outputs are summed and the directional coupler is assumed to be lossless. The fibre to chip coupling loss is de-embedded through an edge coupler measurement.

The extracted Ge PD responsivity is shown in Figure 5.3.

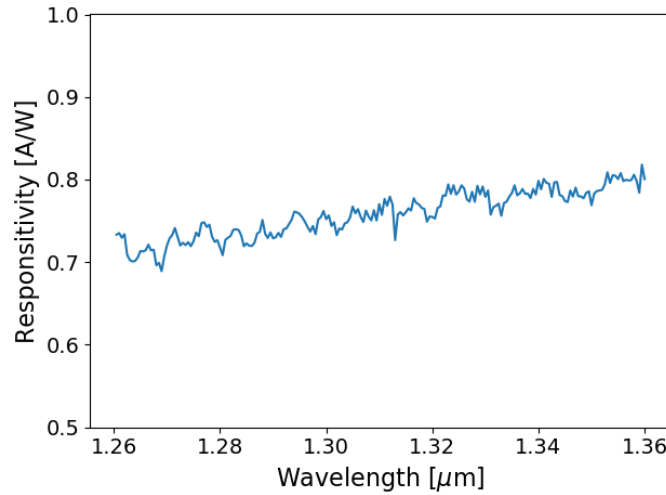


Figure 5.3: *The measured Ge PD responsivity as a function of wavelength.*

The obtained values for the responsivity of $\sim 0.75 \text{ A/W}$ at a reverse bias of -1 V is consistent with previously reported values for Ge PD responsivity in the O-band on a similar platform. [32]

5.4 MMI Measurements

The MMI bar and cross port transmission were characterized through both the cutback and PD test structures described in Chapter 4 in combination with the measured responsivity in Figure 5.3. The results are shown in Figure 5.4.

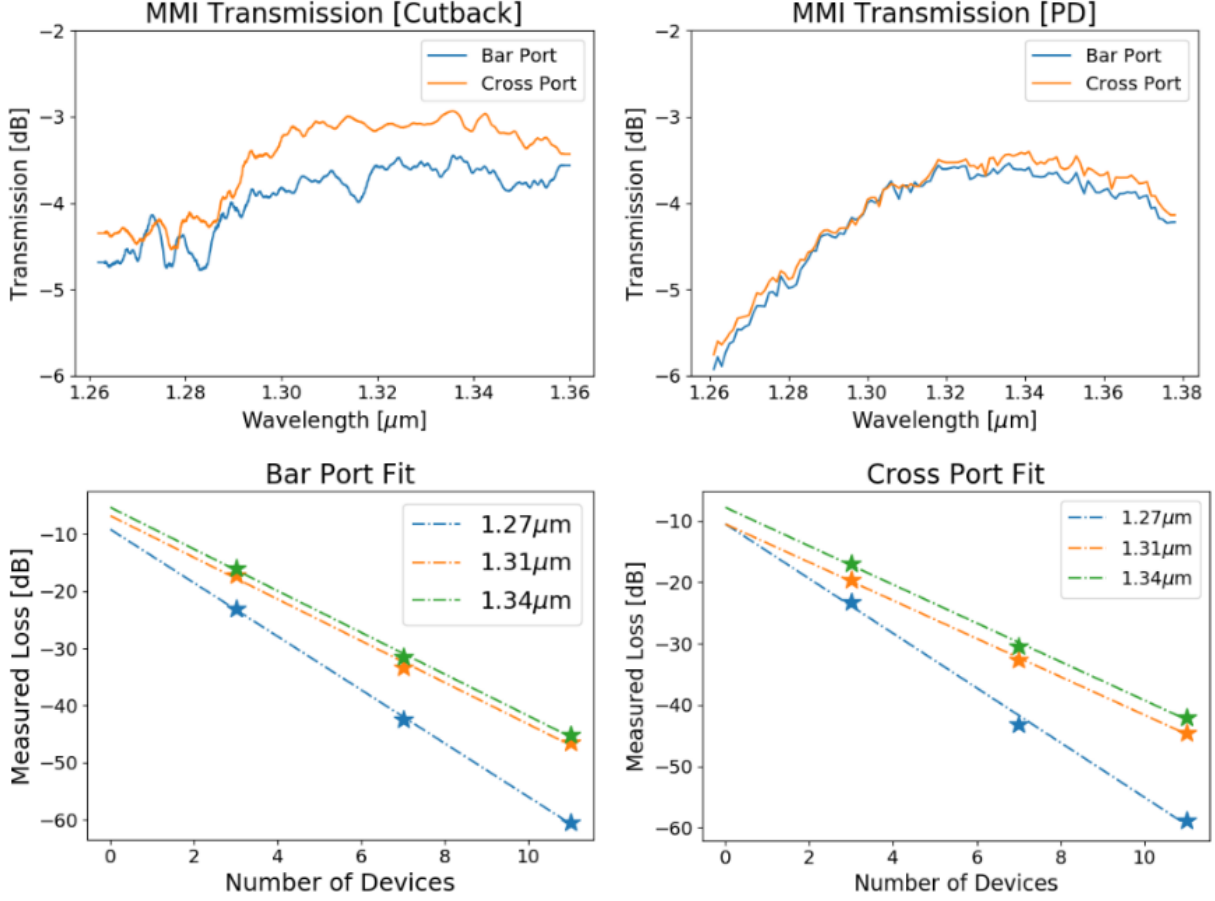


Figure 5.4: MMI characterization results. (top left) cutback characterization (top right) PD characterization (bottom left) raw measurements of bar port cutback measurements at 1.27 μm , 1.31 μm , 1.34 μm (bottom right) raw measurements of cross port cutback measurements at 1.27 μm , 1.31 μm , 1.34 μm

The cutback measurement and the PD measurement show agreement but deviates at shorter wavelengths where insertion loss is higher. This is likely due to the cutback measurements getting close to the noise floor of the detector causing the cutback interpolated transmission to be higher than expected.

The peak performance of the MMI coupler is shifted towards longer wavelengths, which according to the fabrication variation simulation results shown in Chapter 3, indicates possibly a thinner width/height or a higher material index than assumed.

The performance of the MMI coupler in terms of T_{refl} and SPRR as defined in Chapter 3 are shown in Figure 5.5

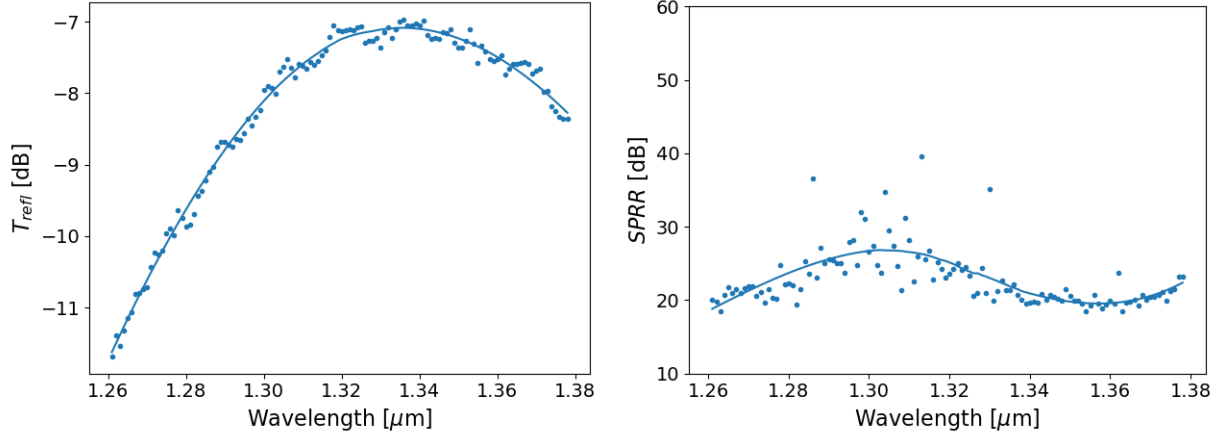


Figure 5.5: Plots of (left) T_{refl} (right) SPRR calculated from the photodetector characterization.

As expected, the MMI coupler performs well in mixing LO and reflections from the DUT in a balanced detection scheme, achieving $>18\text{dB}$ SPRR throughout the measured wavelength range. However, the high insertion losses of the MMI coupler leads to very poor performance when used to isolate the reflections from the DUT, which is compounded by the fact that the peak wavelength of the MMI is shifted, with losses of up to -12dB at shorter wavelengths.

5.5 Directional Coupler Measurements

The raw interferograms measured from the four combinations of inputs and outputs of the UMZI test structure are shown in Figure 5.6.

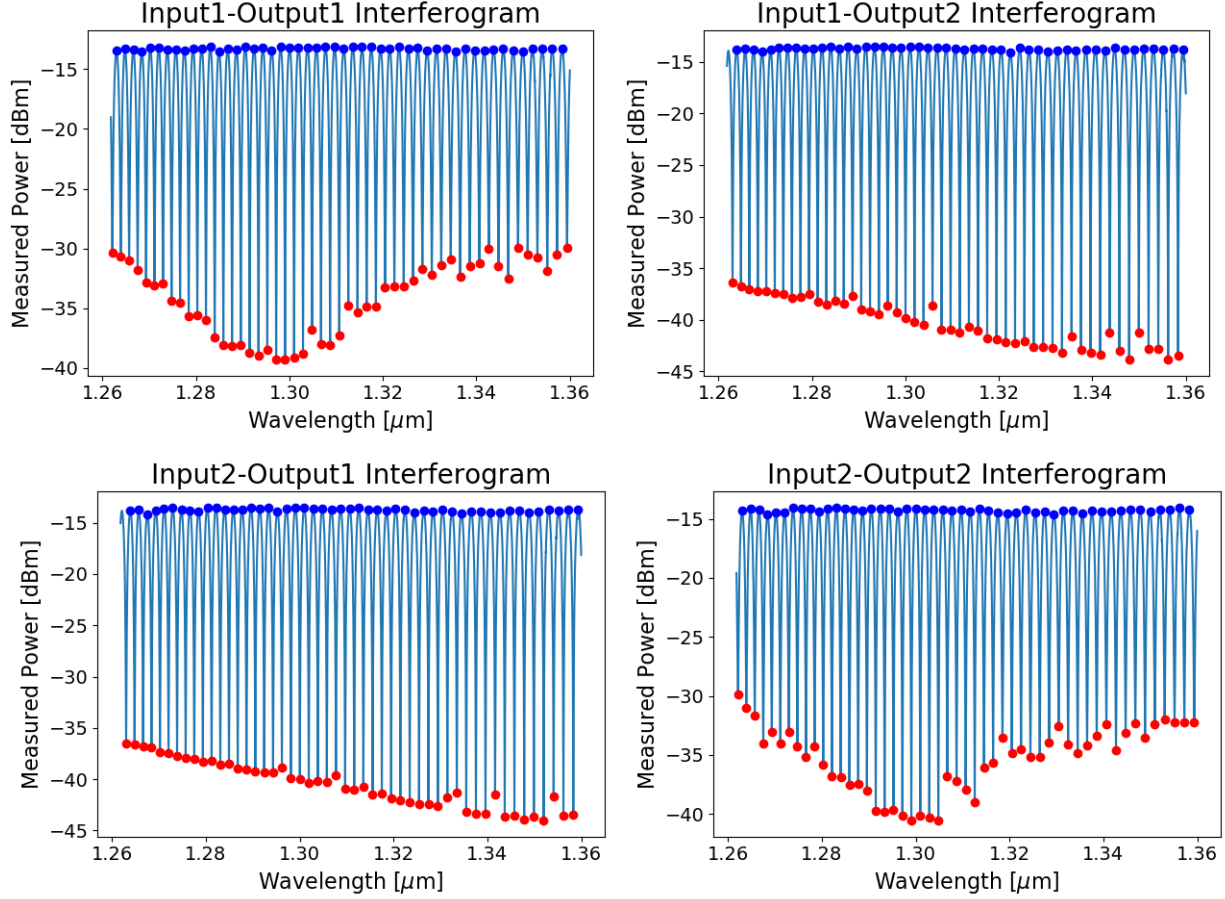


Figure 5.6: Plot of raw data from unbalanced Mach Zehnder interferometer measurement, Blue and red dots indicate the peaks and troughs of the interferogram

From the extinction ratios between the maximas and minimas of interferogram, the bar and cross port transmissions can be extracted from the process detailed in Chapter 4. By comparing the different combination of the interferograms, we can narrow the possible configurations detailed in Chapter 4 by comparing them to the expected excess loss of the longer arm. Through this extraction of the transmissions of the DC, we find that the transmission of the two directional couplers, even though identical on the layout, appears to deviate from each other. The extracted transmissions of the directional coupler through UMZI test structure, as well as the PD test structure are shown in Figure 5.7.

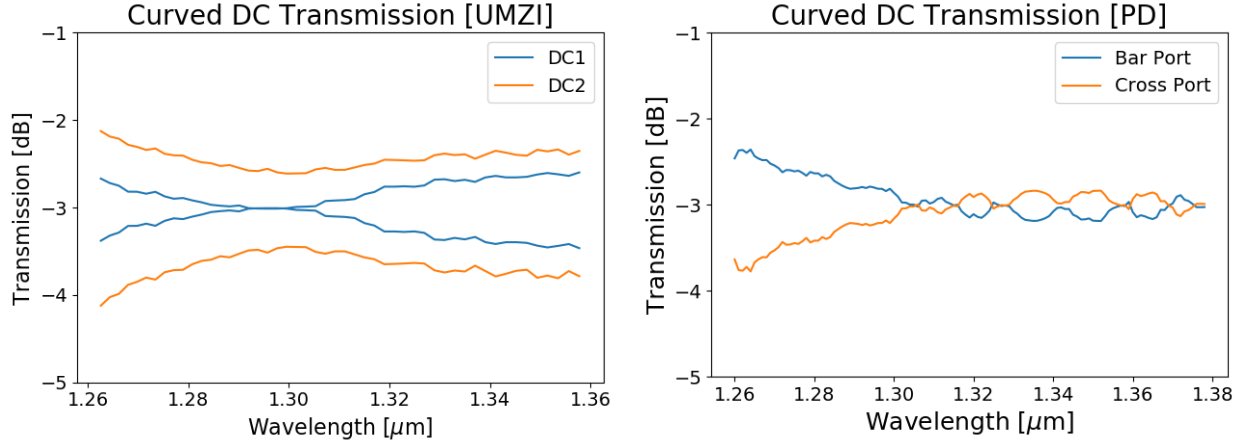


Figure 5.7: Plot of curved directional coupler characterization results. (left) unbalanced Mach Zehnder interferometer characterization, (right) photodetector characterization

Notably, the noise in the extraction of the ER, in combination with the low excess loss on the longer arm of the UMZI test structure made the extraction process detailed in Chapter 4 ambiguous. The PD measurement of the curved DC was used to find the correct values of j, k, l, m in (4.6).

The deviation between the transmissions of the two directional couplers in the UMZI test structure and their deviation from the PD measurement of the transmission of the directional coupler indicates a high fabrication sensitivity. Nevertheless, the flattened wavelength response due to the curvature of the coupling region is clearly present, albeit spectrally shifted towards longer wavelengths, achieving a $3\text{dB} \pm 1\text{dB}$ bandwidth of $>100\text{nm}$, comparable to previous devices reported in the literature and first example of such device on a SiN photonic layer. [40], [51] This combined with the simulation results from Chapter 3, indicates a lower height, wider width or higher index than assumed. The performance of the DC in terms of T_{refl} and SPRR are shown in Figure 5.8.

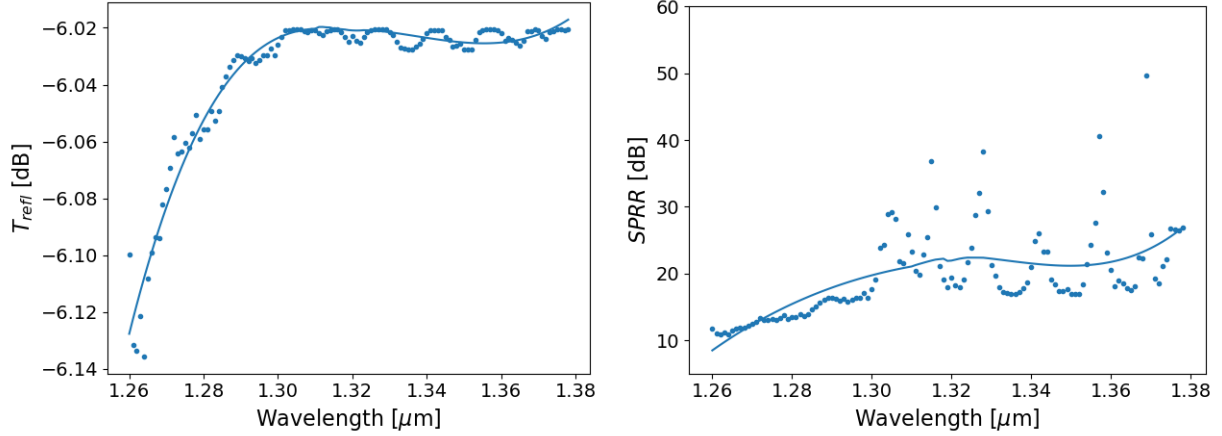


Figure 5.8: Plot of (left) T_{refl} (right) SPRR calculated from the photodetector characterization

As expected, the circulator losses are near optimal, only deviating by 0.1dB from the optimal 6dB of loss for a 2×2 coupler, but the imbalance of the output as the wavelength deviates from the 1:1 point leads to worse performance when interfering the LO and reflections from the DUT for balanced detection compared to the MMI coupler, achieving only >10 dB SPRR in the wavelength range of interest.

5.6 Discussion

The UMZI measurements of DC transmission coefficients were complicated by the fluctuations in the interference pattern formed as wavelength was swept. The fluctuations were likely due to polarization rotation occurring in the $500\mu\text{m}$ long inverse taper edge couplers due to slanted sidewalls that tapers through a square cross-section.[56] The different polarizations in the UMZI arms would have different group indices, leading to unordered overlapping of interference patterns between the TE and TM polarizations. This causes variations in the depths of the troughs as a function of wavelength, especially at low powers ($<-20\text{dBm}$) which leads to uncertainty in the measured ER. A polarization analyzer was added to the measurement setup to minimize this effect, but spectral fluctuation in the extracted ER was still large enough compared to the low excess loss in the longer arm of the UMZI test structure that the identification of the j, k, l, m , coefficients to differentiate

between the different cases mentioned in (4.6) was not possible. The effects of adding a polarization analyzer is shown in Figure 5.9.

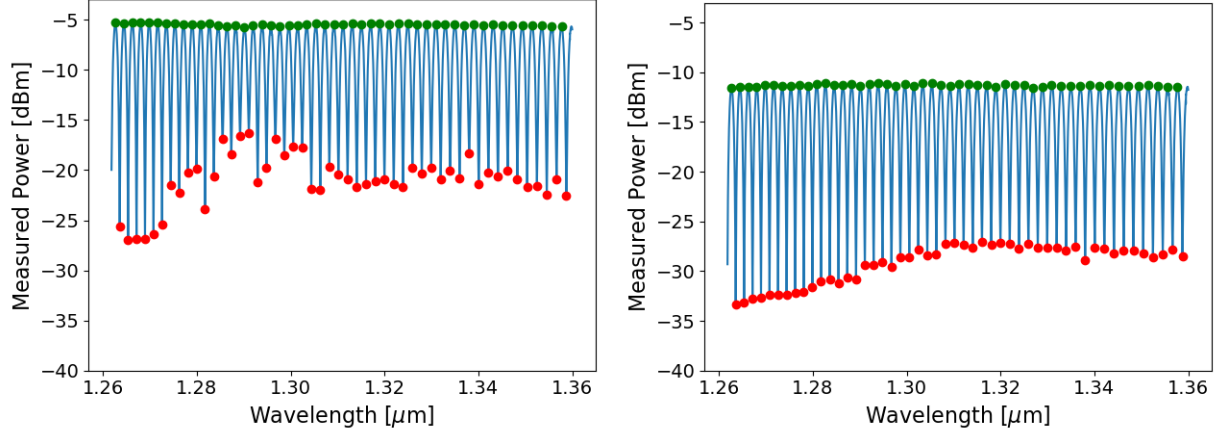


Figure 5.9: Plot of measured unbalanced Mach Zehnder interferometer interference spectra. Green and red dots used to visualize the peaks and troughs (left) Without polarization analyzer (right) With polarization analyzer

In hindsight, a simpler UMZI structure containing a 1x2 MMI as the first coupler and the DC under test as the second coupler would make the extraction of transmission coefficients of the DC simpler, and halve the ER required to make the same measurement, making it less susceptible to the presence of the unwanted polarization.

The cutback measurements for the MMI coupler also had issues with dipping down to the noise floor of the detector due to larger than expected loss. In the future, cutback structures with fewer MMIs should be placed.

5.7 Conclusion

The measured propagation losses for SiN waveguides is much higher than expected, likely due to variations in the composition of the SiN deposited and possibly other fabrication imperfections. The propagation losses for Si were lower than expected, possibly due to reduced surface roughness since the previous value was obtained from the polished top Si device layer in the SOI. Interlayer

transitions insertion loss was lower than expected, which was expected due to reduced scattering losses owing to a smaller blunt tip width and height. The measured Ge PD responsivity was consistent with previously reported results for the O-band.

The bar and cross port transmission for the MMI and curved directional coupler were obtained. The curved directional coupler was sensitive to fabrication variations due to differing transmissions extracted from devices that with identical layouts. The transmission of both the MMI and curved directional coupler were spectrally shifted towards longer wavelengths. The variations that match the spectral shift in the transmission are a higher material index or a reduced height.

Chapter 6

Discussion, Conclusion, and Future Work

In this thesis we designed, optimized, and characterized 2×2 couplers and other general devices as fundamental building blocks for an integrated photonics implementation of OFDR. The 2×2 couplers were designed with two roles in mind. To isolate the back reflected signal of interest from the DUT and to facilitate the interference between that signal and the LO for balanced photodetection. To parameterize the 2×2 coupler performance in isolating the reflections from DUT and interfering signals for balanced detection, T_{refl} and SPRR were defined in Chapter 3. Two candidates for 2×2 couplers, the MMI coupler and curved directional coupler were designed, optimized, fabricated, and characterized through optical and PD test structures with those two parameters in mind.

6.1 Conclusion

The fabricated MMI coupler achieves SPRR >18dB throughout the intended wavelength range.

However, the insertion losses for the isolated reflection from the DUT were severe, reaching up to -12 dB within the targeted wavelength range.

The fabricated curved directional coupler has a near optimal -6.1dB losses for the isolation of reflections from the DUT, but the SPRR only reaches >10dB throughout the intended wavelength range.

The curved directional coupler performs within expected ranges in the presence of fabrication variances simulated in Chapter 3. The MMI SPRR performance is worse than expected in the presence of fabrication variances, however, due to the strong dependence of SPRR on the balance of the output it is more susceptible to fluctuations between the cross and bar port measurements. A comparison of the performance between the characterized MMI and curved DC to other experimentally demonstrated 2×2 couplers on SOI platforms is shown in Table 6.1

Table 6.1: Comparison table for experimentally demonstrated 2×2 couplers on SOI platforms.

Type	Material	1dB Imbalance Bandwidth (THz)	< 1dB Excess Loss Bandwidth (THz)	Footprint ($\mu\text{m} \times \mu\text{m}$)
Adiabatic Coupler w/ subwavelength gratings [54]	Si	>16.2*	>16.2*	1x50
Adiabatic Coupler [53]	Si	>12.5*	Not mentioned	6x1100
Curved Coupler with Straight Sections [51]	Si	11	Not mentioned	3x20
Curved Coupler [40]	Si	15.2	>15.2*	3x20
MMI [57]	Si	>4.1*	Not mentioned	3x9
MMI [58]	Si	>6.2*	>6.9*	4.5x25
This work, curved coupler	SiN	>18.7*	>20.37*	5x30
This work, MMI	SiN	>20.37*	12.42	7x45

*Bandwidth limited by measurement range

Table 6.1 shows that our curved coupler on the SiN-on-Si platform is the most spectrally broadband curved directional coupler demonstrated, with slightly larger device footprints as the Si counterparts, which can be improved in the future. The large bandwidth is owed to the lower dispersion exhibited by the SiN waveguide, with the actual optical bandwidth being even higher than quoted due to limitations in the measurement. Adiabatic couplers in Table 6.1 can reach comparable performance, but either have very large device footprints or require subwavelength features that are not reliably reproduced in foundry fabrication processes. Our MMI on the SiN-on-Si platform shows very large bandwidth with respect to the imbalance of the outputs but has a larger footprint due to the lower

light confinement compared to Si devices. For future iterations, a tapered slab region like the ones described in [59] can be incorporated to further reduce the device footprint.

Optical fibre 2×2 couplers can be very broadband, with 1dB imbalance bandwidth reaching up to 200nm around 1310nm (35.1THz) [60]. However, integrated photonic implementations, when produced on a commercial scale, should have lower costs. Integrated photonic directional couplers should also be free of any insertion losses aside from coupling onto and off the chip, whereas each connector or splice needed for fibre couplers will accrue additional losses.

The advantages and disadvantages of each type of potential on-chip 2×2 coupler are as expected from the simulations from Chapter 3. The results indicate that a hybrid approach using both MMI and curved couplers is optimal for OFDR, where curved directional couplers are used to isolate the back reflections from the DUT and MMI couplers are used for balanced photodetection as shown in Figure 6.1.

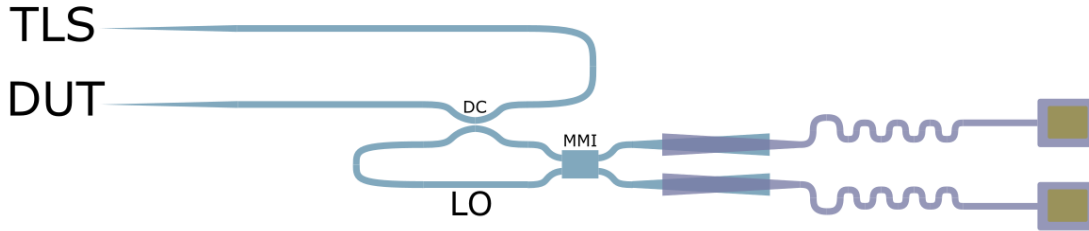


Figure 6.1: Schematic of hybrid configuration of 2×2 couplers for OFDR with the curved directional coupler (DC) routing the light from the tunable laser source (TLS) to the device under test (DUT) and isolating the back reflections from the DUT. and the multimode interferometer (MMI) facilitating the interference between the reflections and the local oscillator (LO).

6.2 Future Work

In this thesis, the basic devices needed for an integrated photonic OFDR circuit have been characterized, and next step involves the combination of all these building blocks into a functioning

prototype of an integrated OFDR with an off-chip light source. To achieve on chip polarization diversity, a polarization splitter rotator can be appended to the OFDR as shown in Figure 6.2.

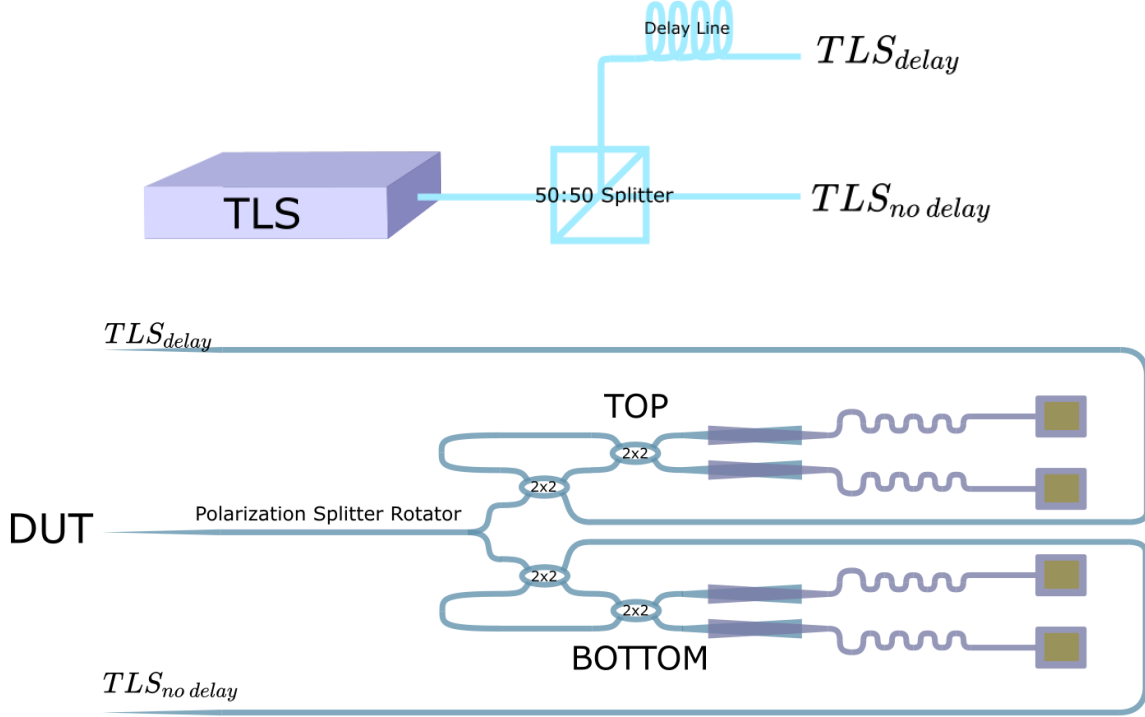


Figure 6.2: Schematic of on chip polarization diversity achieved with integrated polarization splitter rotator (PSR). (top) external bulk optic requirements. Light from the tunable laser source (TLS) is split into 2 paths, with one path connected to a delay line to apply a temporal delay τ (TLS_{delay}) relative to the other path ($TLS_{no\ delay}$). (bottom) photonic circuit: the light travels from TLS_{delay} and $TLS_{no\ delay}$ and is routed towards the device under test (DUT) through the PSR, which converts the TLS_{delay} into the TM polarization. The two polarizations in the back reflections from the DUT are separated by the PSR, and interfered with the local oscillator on the top (originating from TLS_{delay}) and bottom (originating from $TLS_{no\ delay}$) branches of the OFDR. On the top branch, the $TE \rightarrow TM$ and $TM \rightarrow TM$ reflections will have a relative applied delay of $-\tau$ and 0 to the top branch LO respectively. On the bottom branch, the $TE \rightarrow TE$ and $TM \rightarrow TE$ reflections will have a relative applied delay of 0 and τ to the bottom branch LO respectively. The different relative temporal delay in each branch translates to a spatial offset after the interference signal is Fourier transformed, multiplexing the different terms of the reflection's Jones matrix spatially.

By introducing a temporal delay τ to the TE_{delay} input relative to the TE input, each term of the Jones matrix of the reflection will be shifted by the incrementing delays of τ , which manifests as a spatial shift when extracting the locations of the reflection. This adds polarization diversity to the measurement at the cost of maximum range.

Alternatively, polarization insensitive variants of these building blocks with a polarization splitter can be used to obtain polarization specific reflection information if the optical input polarization is varied, similar to [25].

In future iterations, edge couplers can be replaced by grating couplers to utilize the photonic OFDR circuit as a wafer level test structure to characterize wafer index variations and basic devices diagnostics. [61], [62] The photonic integration of OFDR also allows it to take advantage of the offerings of a complex photonics platform, such as thermo-optic tuning of the reference arm of the interferometer to perform multiple scans to improve resolution.

In closing, OFDR is a powerful diagnostic technique that stands to benefit from photonic integration. To implement this on the SiN-on-Si platform, several building blocks, the most important of which is a 2×2 coupler, have been designed, optimized, and characterized. This thesis has also demonstrated the suitability of the SiN-on-Si platform for OFDR due to the combination of the electronic integration of SOI with the passive capabilities of SiN for spectrally broadband components. The next step is the characterization of a fully integrated OFDR photonic circuit.

References

- [1] A. S. Mayer and B. C. Kirkpatrick, "Silicon photonics," *Front. Mod. Opt.*, vol. 24, no. 12, pp. 189–205, 2016.
- [2] A. Barkai *et al.*, "Integrated silicon photonics for optical networks [Invited]," *J. Opt. Netw.*, vol. 6, no. 1, pp. 25–47, 2007.
- [3] P. Dong, X. Liu, S. Chandrasekhar, L. L. Buhl, R. Aroca, and Y. K. Chen, "Monolithic silicon photonic integrated circuits for compact 100 +Gb/s coherent optical receivers and transmitters," *IEEE J. Sel. Top. Quantum Electron.*, vol. 20, no. 4, 2014.
- [4] C. R. Doerr, "Silicon photonic integration in telecommunications," *Front. Phys.*, vol. 3, no. August, pp. 1–16, 2015.
- [5] J. A. Hoerni, "Planar silicon diodes and transistors," *1960 Int. Electron Devices Meet.*, pp. 50–50, 2008.
- [6] A. E. J. Lim *et al.*, "Review of Silicon Photonics Foundry Efforts," *IEEE J. Sel. Top. Quantum Electron.*, vol. 20, no. 4, 2014.
- [7] W. N. Ye and Y. Xiong, "Review of silicon photonics: History and recent advances," *J. Mod. Opt.*, vol. 60, no. 16, pp. 1299–1320, 2013.
- [8] T. Thiessen *et al.*, "Back-Side-on-BOX Heterogeneously Integrated III-V-on-Silicon O-Band Distributed Feedback Lasers," *J. Light. Technol.*, vol. 8724, no. c, pp. 1–1, 2020.
- [9] S. Keyvaninia *et al.*, "Heterogeneously integrated III-V/silicon distributed feedback lasers," *Opt. Lett.*, vol. 38, no. 24, p. 5434, 2013.
- [10] G. Roelkens *et al.*, "III-V-on-silicon photonic devices for optical communication and sensing," *Photonics*, vol. 2, no. 3, pp. 969–1004, 2015.
- [11] T. Y. Liow *et al.*, "Silicon modulators and germanium photodetectors on SOI: Monolithic integration, compatibility, and performance optimization," *IEEE J. Sel. Top. Quantum Electron.*, vol. 16, no. 1, pp. 307–315, 2010.
- [12] W. D. Sacher, Y. Huang, G. Q. Lo, and J. K. S. Poon, "Multilayer silicon nitride-on-silicon integrated photonic platforms and devices," *J. Light. Technol.*, vol. 33, no. 4, pp. 901–910, 2015.
- [13] P. Muñoz *et al.*, "Silicon nitride photonic integration platforms for visible, near-infrared and mid-infrared applications," *Sensors (Switzerland)*, vol. 17, no. 9, pp. 1–25, 2017.
- [14] K. Ikeda, R. E. Saperstein, N. Alic, and Y. Fainman, "Thermal and Kerr nonlinear properties of plasma-deposited silicon nitride/ silicon dioxide waveguides," *Opt. Express*, vol. 16, no. 17, p. 12987, 2008.
- [15] P. E. Ross, "Aeva Unveils Lidar on a Chip," *IEEE Spectrum*, 2019. [Online]. Available: <https://spectrum.ieee.org/cars-that-think/transportation/sensors/lidar-on-a-chip-at-last>. [Accessed: 24-Jan-2020].
- [16] M. Poot, C. Schuck, X. Ma, X. Guo, and H. X. Tang, "Design and characterization of integrated components for SiN photonic quantum circuits," *Opt. Express*, vol. 24, no. 7, p. 6843, 2016.
- [17] P. P. Khial, A. D. White, and A. Hajimiri, "Nanophotonic optical gyroscope with reciprocal sensitivity enhancement," *Nat. Photonics*, vol. 12, no. 11, pp. 671–675, 2018.
- [18] H. Choi and H. F. Taylor, "High-performance fiber-optic temperature sensor using low-coherence interferometry," vol. 22, no. 23, pp. 1814–1816, 1997.
- [19] J. P. Von Der Weid, R. Passy, G. Mussi, and N. Gisin, "On the characterization of optical fiber network components with optical frequency domain reflectometry," *J. Light. Technol.*, vol. 15, no. 7, pp. 1131–1141, 1997.
- [20] A. R. Bahrampour and F. Maasoumi, "Resolution enhancement in long pulse OTDR for

- application in structural health monitoring,” *Opt. Fiber Technol.*, vol. 16, no. 4, pp. 240–249, 2010.
- [21] N. Boujia, F. Schmidt, C. Chevalier, D. Siegert, and D. P. Van Bang, “Distributed optical fiber-based approach for soil–structure interaction,” *Sensors (Switzerland)*, vol. 20, no. 1, pp. 1–14, 2020.
 - [22] J. F. Nascimento, M. J. Silva, I. J. S. Coêlho, E. Cipriano, and J. F. Martins-Filho, “Amplified OTDR systems for multipoint corrosion monitoring,” *Sensors*, vol. 12, no. 3, pp. 3438–3448, 2012.
 - [23] A. Kowalewicz, T. Ko, I. Hartl, J. Fujimoto, M. Pollnau, and R. Salathé, “Ultrahigh resolution optical coherence tomography using a superluminescent light source,” *Opt. Express*, vol. 10, no. 7, p. 349, 2002.
 - [24] Y. Wang, Y. Zhao, J. S. Nelson, Z. Chen, and R. S. Windeler, “Ultrahigh-resolution optical coherence tomography by broadband continuum generation from a photonic crystal fiber,” *Opt. Lett.*, vol. 28, no. 3, p. 182, 2003.
 - [25] B. J. Soller, D. K. Gifford, M. S. Wolfe, and M. E. Froggatt, “High resolution optical frequency domain reflectometry for characterization of components and assemblies,” *Opt. Express*, vol. 13, no. 2, p. 666, 2005.
 - [26] F. Ito, X. Fan, and Y. Koshikiya, “Long-range coherent OFDR with light source phase noise compensation,” *J. Light. Technol.*, vol. 30, no. 8, pp. 1015–1024, 2012.
 - [27] W. D. Sacher, T. Barwicz, B. J. F. Taylor, and J. K. S. Poon, “Polarization rotator-splitters in standard active silicon photonics platforms,” *Opt. Express*, vol. 22, no. 4, p. 3777, 2014.
 - [28] H. Fukuda, K. Yamada, T. Tsuchizawa, T. Watanabe, H. Shinojima, and S. Itabashi, “Ultrasmall polarization splitter based on silicon wire waveguides,” *Opt. Express*, vol. 14, no. 25, p. 12401, 2006.
 - [29] R. C. Haskell *et al.*, “Role of beat noise in limiting the sensitivity of optical coherence tomography,” *J. Opt. Soc. Am. A*, vol. 23, no. 11, p. 2747, 2006.
 - [30] Y. Painchaud, M. Poulin, M. Morin, and M. Têtu, “Performance of balanced detection in a coherent receiver,” *Opt. Express*, vol. 17, no. 5, p. 3659, 2009.
 - [31] Y. Huang, J. Song, X. Luo, T.-Y. Liow, and G.-Q. Lo, “CMOS compatible monolithic multi-layer Si₃N₄-on-SOI platform for low-loss high performance silicon photonics dense integration,” *Opt. Express*, vol. 22, no. 18, p. 21859, 2014.
 - [32] W. D. Sacher *et al.*, “Monolithically Integrated Multilayer Silicon Nitride-on-Silicon Waveguide Platforms for 3-D Photonic Circuits and Devices,” *Proc. IEEE*, vol. 106, no. 12, pp. 2232–2245, 2018.
 - [33] R. Larrea, A. M. Gutierrez, A. Griol, A. Brimont, and P. Sanchis, “Fiber-to-Chip Spot-Size Converter for Coupling to Silicon Waveguides in the O-Band,” *IEEE Photonics Technol. Lett.*, vol. 31, no. 1, pp. 31–34, 2019.
 - [34] J. Cardenas, K. Luke, L. W. Luo, C. B. Poitras, P. A. Morton, and M. Lipson, “High coupling efficiency etched facet tapers in silicon,” *Opt. InfoBase Conf. Pap.*, vol. 26, no. 23, pp. 2380–2382, 2012.
 - [35] Corning Product Information, “Corning SMF-28 Ultra Optical Fiber,” no. November, pp. 1–2, 2014.
 - [36] R. Sun *et al.*, “Impedance matching vertical optical waveguide couplers for dense high index contrast circuits,” *Opt. Express*, vol. 16, no. 16, p. 11682, 2008.
 - [37] W. D. Sacher *et al.*, “Tri-layer silicon nitride-on-silicon photonic platform for ultra-low-loss crossings and interlayer transitions,” *Opt. Express*, vol. 25, no. 25, p. 30862, 2017.
 - [38] K. Shang, S. Pathak, B. Guan, G. Liu, and S. J. B. Yoo, “Low-loss compact multilayer silicon nitride platform for 3D photonic integrated circuits,” *Opt. Express*, vol. 23, no. 16, p. 21334, 2015.
 - [39] J. Wang *et al.*, “Evanescent-coupled Ge p-i-n photodetectors on Si-waveguide with SEG-Ge and comparative study of lateral and vertical p-i-n configurations,” *IEEE Electron Device Lett.*, vol. 29, no. 5, pp. 445–448, 2008.
 - [40] S. Chen, Y. Shi, S. He, and D. Dai, “Low-loss and broadband 2 × 2 silicon thermo-optic Mach–

- Zehnder switch with bent directional couplers,” *Opt. Lett.*, vol. 41, no. 4, p. 836, Feb. 2016.
- [41] J. C. Mikkelsen, A. Bois, T. Lordello, D. Mahgerefteh, S. Menezo, and J. K. S. Poon, “Polarization-insensitive silicon nitride Mach-Zehnder lattice wavelength demultiplexers for CWDM in the O-band,” *Opt. Express*, vol. 26, no. 23, p. 30076, 2018.
 - [42] Z. Yong *et al.*, “U-shaped PN junctions for efficient silicon Mach-Zehnder and microring modulators in the O-band: erratum,” *Opt. Express*, vol. 26, no. 25, p. 32757, 2018.
 - [43] B. J. Soller, D. K. Gifford, M. S. Wolfe, and M. E. Froggatt, “High resolution optical frequency domain reflectometry for characterization of components and assemblies,” *Opt. Express*, vol. 13, no. 2, p. 666, 2005.
 - [44] L. B. Soldano and E. C. M. Pennings, “Optical Multi-Mode Interference Devices Based on Self-Imaging: Principles and Applications,” *J. Light. Technol.*, vol. 13, no. 4, pp. 615–627, 1995.
 - [45] P. A. Besse, M. Bachmann, H. Melchior, L. B. Soldano, and M. K. Smit, “Optical Bandwidth and Fabrication Tolerances of Multimode Interference Couplers,” *J. Light. Technol.*, vol. 12, no. 6, pp. 1004–1009, 1994.
 - [46] A. Takagi, K. Jinguji, and M. Kawachi, “Wavelength characteristics of (2×2) optical channel-type directional couplers with symmetric or nonsymmetric coupling structures,” *J. Light. Technol.*, vol. 10, no. 6, pp. 735–746, Jun. 1992.
 - [47] W.-P. Huang, “Coupled-mode theory for optical waveguides: an overview,” *J. Opt. Soc. Am. A*, vol. 11, no. 3, p. 963, 1994.
 - [48] C. R. Doerr *et al.*, “Bending of a planar lightwave circuit 2 × 2 coupler to desensitize it to wavelength, polarization, and fabrication changes,” *IEEE Photonics Technol. Lett.*, 2005.
 - [49] L. Leick, J. H. Povlsen, and R. J. S. Pedersen, “Achieving small process tolerant wavelength-flattened 3 dB directional couplers in Silica-on-Silicon,” in *Integrated Photonics Research*, 2000, p. IThB6.
 - [50] H. Morino, T. Maruyama, and K. Iiyama, “Reduction of wavelength dependence of coupling characteristics using Si optical waveguide curved directional coupler,” *J. Light. Technol.*, vol. 32, no. 12, pp. 2188–2192, 2014.
 - [51] S. T. Lim, T. Y. L. Ang, G. F. R. Chen, D. T. H. Tan, C. E. Png, and J. R. Ong, “Broadband Silicon-On-Insulator directional couplers using a combination of straight and curved waveguide sections,” *Sci. Rep.*, 2017.
 - [52] K. Solehmainen, M. Kapulainen, M. Harjanne, and T. Aalto, “Adiabatic and Multimode Interference Couplers on Silicon-on-Insulator,” *IEEE Photonics Technol. Lett.*, vol. 18, no. 21, pp. 2287–2289, Nov. 2006.
 - [53] M. A. Tran, C. Zhang, and J. E. Bowers, “A broadband optical switch based on adiabatic couplers,” *2016 IEEE Photonics Conf. IPC 2016*, pp. 755–756, 2017.
 - [54] H. Yun *et al.*, “Broadband 2 × 2 adiabatic 3 dB coupler using silicon-on-insulator sub-wavelength grating waveguides,” *Opt. Lett.*, vol. 41, no. 13, p. 3041, 2016.
 - [55] M. A. Tran, T. Komljenovic, J. C. Hulme, M. L. Davenport, and J. E. Bowers, “A Robust Method for Characterization of Optical Waveguides and Couplers,” vol. 28, no. 14, pp. 1517–1520, 2016.
 - [56] L. Jia *et al.*, “Analysis of the polarization rotation effect in the inversely tapered spot size converter,” *Opt. Express*, vol. 23, no. 21, p. 27776, 2015.
 - [57] D.-X. Xu *et al.*, “High bandwidth SOI photonic wire ring resonators using MMI couplers,” *Opt. Express*, vol. 15, no. 6, p. 3149, 2007.
 - [58] Y. Zhang, M. Schneider, L. Eisenblätter, D. Karnick, T. Kühner, and M. Weber, “Multimode interferometers for integrated transceivers on 250 nm SOI platform,” *J. Instrum.*, vol. 15, no. 02, pp. P02022–P02022, Feb. 2020.
 - [59] A. Hosseini, D. N. Kwong, H. Subbaraman, and R. T. Chen, “Demonstration of compact 2×2 multimode interference coupler on silicon nanomembrane,” *IEEE Int. Conf. Gr. IV Photonics GFP*, vol. 1, no. 1, pp. 263–265, 2010.

- [60] Thorlabs, “1310 nm 2×2 Single Mode Fused Fiber Optic Couplers / Taps,” 2018. [Online]. Available: https://www.thorlabs.com/newgrouppage9.cfm?objectgroup_id=8461. [Accessed: 27-Sep-2020].
- [61] D. Melati, A. Alippi, and A. Melloni, “Waveguide-based technique for wafer-level measurement of phase and group effective refractive indices,” *J. Light. Technol.*, vol. 34, no. 4, pp. 1293–1299, 2016.
- [62] D. Zhao, D. Pustakhod, K. Williams, and X. Leijtens, “High Resolution Optical Frequency Domain Reflectometry for Analyzing Intra-Chip Reflections,” *IEEE Photonics Technol. Lett.*, vol. 29, no. 16, pp. 1379–1382, Aug. 2017.